

STRUCTURED GENERATIVE MODELING WITH THE THERMODYNAMIC KOLMOGOROV-ARNOLD MODEL

Prithvi Raj

The Zettascale Computing Corp. *

prithvi@zscc.ai

ABSTRACT

Learning an energy-based model (EBM) in the latent space of a top-down generative model offers a versatile framework for generation across multiple data modalities. However, it remains unclear how its interpretability can be used to guide model design, improve generative quality, and reduce training time. Moreover, the reliance on Langevin Monte Carlo (LMC) sampling presents challenges in efficiency and sampling multimodal latent distributions. In this work, we propose a novel adaptation of the Kolmogorov-Arnold representation theorem for generative modeling and introduce the Thermodynamic Kolmogorov-Arnold Model (T-KAM) to take advantage of structural and inductive biases. By constraining the prior to univariate relationships, T-KAM enables fast and exact inference via the inverse transform method. With the low dimensionality of the latent space and suitable inductive biases encoded, we demonstrate that importance sampling (IS) becomes a viable, unbiased, and highly efficient posterior sampler. For situations where IS fails, we investigate a novel strategy using population-based LMC, which decomposes posterior sampling into a sequence of annealed distributions to improve multimodal sampling. T-KAM elegantly balances common trade-offs in generative modeling, offering fast inference, interpretability, and stable training, while being naturally suited to upcoming Zettascale Computing Corp. hardware.

1 INTRODUCTION

Deep generative modeling is a core subfield of machine learning that enables systems to learn complex data distributions, generate novel data, and support a wide range of tasks including simulation, compression, and representation learning. Two prominent and widely studied approaches are Variational Autoencoders (VAEs) (Kingma & Welling, 2022) and Generative Adversarial Networks (GANs) (Goodfellow et al., 2014). Both frameworks assume that each data point is generated from a low-dimensional latent vector via a top-down neural network, where the latent vector is typically drawn from a simple, non-informative prior, such as a uniform or isotropic Gaussian distribution.

Latent energy-based prior models (EBMs) (Pang et al., 2020) extend this framework by learning an expressive, data-dependent prior directly in the latent space. This prior can be trained jointly with the top-down generator using maximum likelihood estimation (MLE), where the EBM learns by the statistical discrepancy between samples from the prior and posterior distributions, following a paradigm similar to Empirical Bayes. Each learning iteration requires Markov Chain Monte Carlo (MCMC) sampling from both the prior and posterior, specifically the Unadjusted Langevin Algorithm (ULA) (Brooks et al., 2011; Rossky et al., 1978b; Roberts & Stramer, 2002), which offers greater modeling flexibility compared to the amortized inference methods of VAEs.

Despite being extendable to several high-impact research directions, such as multimodal generative modeling (Yuan et al., 2024), and interpretable classification and meta-learning (Kong et al., 2021), (which involves rapid adaptability and few-shot generalization to out-of-distribution tasks), latent EBMs face critical limitations due to their reliance on MCMC sampling.

Firstly, MCMC is inherently iterative, and algorithms such as ULA require repeated gradient passes through the model, which introduces significant computational overhead during both training and

*Previously Exa Laboratories

inference. Secondly, ULA is best suited for sampling from smooth, unimodal distributions and can struggle to explore the multimodal latent distributions that are typical in latent variable generative modeling. Moreover, the framework presented by Pang et al. (2020) requires separate ULA samplers for the prior and posterior. This introduces additional experimental complexity since ULA is sensitive to hyperparameter tuning: step sizes that are too small lead to poor mixing and convergence, while larger step sizes can accumulate discretization bias due to its use of the Euler-Maruyama method (Wilkie, 2004) to evolve the underlying Langevin equation.

Additionally, it is not evident how the unique separation between the prior and generator networks can be leveraged for interpretability or training efficiency. Unlike the framework introduced by Karniadakis et al. (2021), which describes how scientific inductive and learning biases can be embedded into neural networks to reduce their reliance on data and improve training efficiency, generalization, and explainability, (all of which are critical for ensuring trust in Artificial Intelligence), it remains unclear how the EBM prior can be effectively aligned with the posterior to achieve similar effects. Although ideas from mechanistic interpretability, as reviewed by Bereska & Gavves (2024), could potentially be applied, there is currently no established method to leverage the unique strengths of the EBM prior framework for this purpose.

1.1 INDUCTIVE BIASES AND FAST SAMPLING

To address these limitations, we reimagine the EBM prior into a novel univariate or element-wise model, drawing inspiration from Kolmogorov-Arnold Networks (KANs) (Liu et al., 2024) and deep spline networks Bohra et al. (2020), which replace the sigmoidal activations used in multilayer perceptrons Murtagh (1991) with spline interpolations. By representing the latent space with univariate functions and distributions, we enable fast and exact prior sampling with the inverse transform method (Devroye, 1986) and improve interpretability for domain experts who may not be deeply familiar with computational statistics and machine learning. This allows the EBM prior to be aligned with the posterior before training begins.

In Sec. 3.1, we show that adequately chosen priors can enable efficient training with importance sampling (IS) (Goertzel, 1949). This is a technique for estimating posterior expectations that is otherwise avoided in the literature due to its high variance under severe prior-posterior mismatch and the curse of dimensionality, (Dupuis & Wang, 2004), which can be avoided in our model due to the low dimensionality of the latent space. Moreover, we show that the trained priors are easy to visualize and recover, offering new opportunities for scientific discovery and knowledge transfer to models with different latent structures.

Multiple KAN bases and reference priors were used to verify the effect of inductive bias on training with IS. However, Gaussian Radial Basis Functions (RBF KANs) (Li, 2024), were adopted instead of the cubic B-spline bases proposed by Liu et al. (2024), as RBFs are more efficient for GPU implementation, and Poggio & Girosi (1990) previously demonstrated that they provide an optimal solution to the regularized approximation/interpolation problem.

To derive our new model, which we call the Thermodynamic Kolmogorov-Arnold Model (T-KAM), we first introduce a novel adaptation of the Kolmogorov-Arnold Representation Theorem (KART) (Givental et al., 2009) by reinterpreting its inner functions as Markov kernels between probability spaces. Given its finite and definitive nature, KART can provide structural bias and reduce the reliance of architecture design on intuition and automated tuning.

This reinterpretation allows us to frame inverse transform sampling (ITS) as a measurable transformation applied to uniform noise, thus preserving the deterministic structure of KART while admitting a probabilistic interpretation that aligns with MLE. To address the potential inflexibility of strict adherence to KART and the limitations of using independent energy-based priors, we introduce a scalable strategy based on mixture distributions. Beyond introducing dependencies between latent dimensions to capture inter-dimensional relationships, this also improves sampling efficiency by enabling component-wise sampling.

1.2 POPULATION-BASED LANGEVIN SAMPLING AND THERMODYNAMIC TRAINING

However, while ITS enables fast inference, posterior sampling must still be conducted using ULA when the IS estimator is insufficient. Prior work addressing poor MCMC convergence and multi-

modal exploration in EBMs has typically relied on diffusion models, such as the hierarchical EBM by Cui & Han (2024) and the diffusion-assisted EBM by Zhang et al. (2023). To maintain prior interpretability and fast inference post-training, we instead introduce posterior annealing as a novel and alternative strategy. This involves decomposing the posterior into a sequence of power posteriors, presented by Friel & Pettitt (2008), and recasting ULA with population-based MCMC methods (Swendsen & Wang, 1986; Marinari & Parisi, 1992; Hukushima & Nemoto, 1996).

The resulting training criterion is derived from the discretized Thermodynamic Integral and the Steppingstone Estimator (SE), as presented by Calderhead & Girolami (2009); Annis et al. (2019) to ensure the impact of annealing on learning dynamics and parameter updates. Although this reduces expressivity compared to hierarchical EBMs, it ensures that inductive biases remain easy to embed into the latent prior and interpret after training; and unlike denoising, annealing is embarrassingly parallel.

While ULA is computationally efficient and enables more flexible chain dynamics, it does not preserve detailed balance or reversibility. This can be recovered by incorporating Metropolis-Hastings (MH) adjustments (Metropolis & Ulam, 1949) via the Metropolis-adjusted Langevin Algorithm (MALA) (Rossky et al., 1978a). The code in Sec. A.1 optionally supports MALA with locally adaptive step-size tuning, (autoMALA) (Biron-Lattes et al., 2024), to assist when a single step size fails to accommodate the varying geometries of power posteriors, and when the MH criterion deteriorates under the curse of dimensionality, (Hairer et al., 2014). This is discussed in Secs. A.6.3 and A.6.4.

However, ULA remains the preferred method in our work, motivated by its efficiency and effectiveness, demonstrated by Pang et al. (2020) and further supported by the findings of Nijkamp et al. (2019b;a), with regards to how short-run, biased MCMC methods can still be highly effective for sampling from EBMs.

MLE and SE are compared in Sec. 3.2. Despite our optimizations, the element-wise and localized nature of KANs complicate their parallelization on GPUs, which are best suited to matrix arithmetic. As a result, forward passes through T-KAM and the gradient evaluations required for ULA were found to be slow, necessitating reduced experimental complexity.

The experiments in Sec. 3.2 demonstrate that our mixture prior model is able to generate coherent, (although low-quality), samples after a few training epochs on RGB images, while still supporting efficient, exact sampling via component-wise ITS. In contrast, annealing incurred substantial computational overhead, but produced little to no improvements in sample quality, rendering its use difficult to justify. However, this result may change as a larger number of power posteriors, longer training durations, and more advanced posterior sampling algorithms become practical with the hardware advances proposed by Zetta (2024). Their architecture enables fine-grained control over data flow and parallelized element-wise nonlinearity which is naturally well suited to supporting T-KAM at scale, while improving the potential of univariate priors with its function fusion features.

We present T-KAM as an initial step to inspire further adaptations of KART in machine learning. This work aims to lay the groundwork for more exploration amongst the research community, with the far-reaching hope of eventually advancing towards a broader conceptualization: *“The Kolmogorov-Arnold Representation Theorem Is All You Need.”*

2 THE THERMODYNAMIC KOLMOGOROV-ARNOLD MODEL

This section introduces the model and its associated sampling procedures. We begin by presenting a novel interpretation of the Kolmogorov-Arnold Representation Theorem (KART) to define the model’s baseline architecture. Our key practical contribution is the introduction of a univariate energy-based prior, detailed in Sec. 2.1. The top-down generator can be instantiated in various forms, including Kolmogorov-Arnold Networks (KANs), which enables strict adherence to KART.

We then propose scalable extensions to the model, including mixture distributions in Sec. 2.3.2, which introduce dependencies between latent dimensions. This represents a novel contribution to the literature on EBM priors. The final sections address prior and posterior sampling: we introduce inverse transform sampling (ITS) as a new approach for efficient EBM prior sampling, and introduce the posterior annealing strategy in Sec. 2.5 to improve multimodal sampling during training.

The Kolmogorov-Arnold Representation theorem (KART) (Givental et al., 2009) forms the basis of T-KAM. A structured proof of the theorem has been provided by Dzhenzher & Skopenkov (2022).

The Kolmogorov-Arnold Representation theorem 1 *For any integer $n_z > 1$, there are continuous univariate functions $\Phi_q : \mathbb{R} \rightarrow \mathbb{R}$ and $\psi_{q,p} : [0, 1] \rightarrow \mathbb{R}$, such that any continuous multivariate function, $g : [0, 1]^{n_z} \rightarrow \mathbb{R}$, can be represented as a superposition of those functions:*

$$g(u_1, \dots, u_{n_z}) = \sum_{q=1}^{2n_z+1} \Phi_q \left(\sum_{p=1}^{n_z} \psi_{q,p}(u_p) \right), \quad (1)$$

Eq. 1 can provide structural bias and guide the design of T-KAM’s architecture. To ensure adherence to it, any transformations must be derived to be continuous, measurable, and deterministic. For readers less familiar with the technical background, the two most practically significant equations of Sec. 2.1 are Eqs. 4 & 6.

2.1 UNIVARIATE ENERGY-BASED PRIOR

We interpret $u_p \sim \mathcal{U}(u_p; 0, 1)$ in Eq. 1 as a uniform random variable in the probability space, $([0, 1], \mathcal{B}([0, 1]), \mu)$, where $\mathcal{B}([0, 1])$ is the Borel σ -algebra on $[0, 1]$ and μ is the Lebesgue measure on $[0, 1]$. To ensure that the transformation $u_p \mapsto \psi_{q,p}(u_p)$ is well defined in a probabilistic setting, we require it to be a Markov kernel. For all Borel measurable sets $A \subseteq \mathcal{Z}$, where $\mathcal{Z} \subset \mathbb{R}$ is introduced as the latent space of T-KAM, the map

$$u_p \mapsto K(u_p, A) = \delta_{\psi_{q,p}(u_p)}(A) \quad (2)$$

is measurable. Here, $\delta_{\psi_{q,p}(u_p)}$ denotes the Dirac measure centred at $\psi_{q,p}(u_p)$, ensuring the kernel is deterministic: i.e., once u_p is sampled, the outcome in \mathcal{Z} is fixed. This guarantees that the pushforward from $([0, 1], \mathcal{B}([0, 1]), \mu)$ to $(\mathcal{Z}, \mathcal{B}(\mathcal{Z}), \pi)$ is well defined and that no additional stochasticity is introduced beyond the uniform source variable, u_p . Here, $\mathcal{B}(\mathcal{Z})$ is the Borel σ -algebra on the latent space, \mathcal{Z} , and π is the latent measure.

The functions $\psi_{q,p}$ can therefore be conveniently interpreted as inverse cumulative distribution functions (CDFs) corresponding to independent univariate priors:

$$\psi_{q,p}(u_p) = F^{-1}(\pi_{q,p})(u_p). \quad (3)$$

Here, $F^{-1}(\pi_{q,p}) : [0, 1] \rightarrow \mathcal{Z}$ is the generalized inverse CDF associated with a parameterized latent distribution, $\pi_{q,p}$. This is valid under standard regularity assumptions on F , since it is a measurable, monotone, increasing function, and thus $F^{-1}(u) = \inf \{z \in \mathcal{Z} : F(z) \geq u\}$ is a measurable mapping between the two probability spaces. We parameterize the latent distribution $\pi_{q,p}$ via exponential tilting of a base prior π_0 :

$$\pi_{q,p}(z) = \frac{\exp(f_{q,p}(z))}{Z_{q,p}} \pi_0(z), \quad (4)$$

where $f_{q,p}(z)$ is a learned energy function and $Z_{q,p}$ is the normalizing constant (partition function) that ensures $\pi_{q,p}$ defines a valid probability. The inspiration for this exponential tilting form can be traced to the energy-based prior introduced by Pang et al. (2020), adapted to the univariate case. The base prior π_0 serves as a reference measure that guides the form of the learned distribution $\pi_{q,p}$, allowing for flexible reweighting via the energy function $f_{q,p}$.

For $\pi_{q,p}$ to define a valid probability distribution, it must satisfy countable additivity while being non-negative and normalized. This is guaranteed since $f_{q,p} : \mathcal{Z} \rightarrow \mathbb{R}$ is Borel-measurable and integrable with respect to the reference density π_0 , ensuring the finiteness of the partition function:

$$Z_{q,p} = \int_{\mathcal{Z}} \exp(f_{q,p}(z)) d\pi_0(z) < \infty. \quad (5)$$

In practice, $f_{q,p}$ can be parameterized in various ways, made possible by the recent development of Kolmogorov-Arnold Networks (KANs) (Liu et al., 2024). For instance, smoothing splines, such as those used by KANs or deep spline networks, (Bohra et al., 2020). Splines are typically defined on bounded domains, allowing the support of $\pi_{q,p}$ to be explicitly controlled by the user.

The partition function $Z_{q,p}$ is often intractable in energy-based models. However, in this univariate setting, where the energy function is smooth and defined on a bounded domain $[z_{\min}, z_{\max}]$, it can be accurately approximated using Gauss-Kronrod quadrature, (Laurie, 1997):

$$Z_{q,p} = \int_{z_{\min}}^{z_{\max}} \exp(f_{q,p}(z)) \pi_0(z) dz \approx \sum_{i=1}^{N_{\text{quad}}} w_i, G(z_i^{\text{node}}), \quad (6)$$

where $G(z) = \exp(f_{q,p}(z)) \pi_0(z)$, and $\{z_i^{\text{node}}, w_i\}_{i=1}^{N_{\text{quad}}}$ are the quadrature nodes and weights for the interval $[z_{\min}, z_{\max}]$. The smoothness of G , together with its bounded support, makes this approximation highly accurate.

With an valid form for the normalized CDF, inverse transform sampling (ITS) can be used to draw samples from $\pi_{q,p}$ as deterministic transformations of uniform noise. This preserves the deterministic structure of KART while enabling flexible, learnable latent distributions. Inverse transform sampling remains effective even for functions that are not Riemann integrable, provided they are integrable in the Lebesgue sense, typical for the functions in KAN literature.

As a result, the model retains a coherent probabilistic interpretation of KART that is consistent with the energy-based framework proposed by Pang et al. (2020), which is well suited to maximum likelihood training. However, this approach is significantly limited, as it ignores inter-dimensional dependencies in the latent space and results in an axis-aligned joint distribution. We address this inflexibility in Sec. 2.3.2 by relaxing our adherence to KART.

2.2 KOLMOGOROV-ARNOLD NETWORK GENERATOR

Having sampled the intermediary latent variable with ITS such that $z_{q,p} = F^{-1}(\pi_{q,p})(u_p)$, the generator can be realized flexibly as $\mathcal{G} : \mathcal{Z} \rightarrow \mathcal{X}$:

$$\tilde{\mathbf{x}}^{(s)} = \mathcal{G} \left(\mathbf{z}^{(s)} \right) + \boldsymbol{\epsilon}^{(s)}, \quad \text{where } z_{q,p}^{(s)} \sim \pi_{q,p}(z), \quad \boldsymbol{\epsilon}^{(s)} \sim \mathcal{N}(\boldsymbol{\epsilon}; \mathbf{0}, \sigma_\epsilon^2 \mathbf{I}), \quad (7)$$

where $\tilde{\mathbf{x}}^{(s)} = \{\tilde{x}_o^{(s)}\}_{o=1}^{n_x}$ represents a generated data sample corresponding to a single latent sample indexed by s , and n_x is used to specify the dimension of $\tilde{\mathbf{x}}^{(s)}$. The additive noise is a Gaussian sample with hyperparameter σ_ϵ . However, the architecture may be made strictly adherent to KART using a Kolmogorov-Arnold Network:

$$\tilde{x}_o^{(s)} = \sum_{q=1}^{2n_z+1} \Phi_{o,q} \left(\sum_{p=1}^{n_z} z_{q,p}^{(s)} \right) + \epsilon_o^{(s)}, \quad \tilde{\mathbf{x}}^{(s)} = \begin{pmatrix} \sum_{q=1}^{2n_z+1} \Phi_{1,q} \left(\sum_{p=1}^{n_z} z_{q,p}^{(s)} \right) \\ \sum_{q=1}^{2n_z+1} \Phi_{2,q} \left(\sum_{p=1}^{n_z} z_{q,p}^{(s)} \right) \\ \vdots \\ \sum_{q=1}^{2n_z+1} \Phi_{n_x,q} \left(\sum_{p=1}^{n_z} z_{q,p}^{(s)} \right) \end{pmatrix} + \boldsymbol{\epsilon}^{(s)}. \quad (8)$$

The functions, $\Phi_{o,q} : \mathbb{R} \rightarrow \mathbb{R}$, are realizable as basis or KAN functions similar to $f_{q,p} : \mathcal{Z} \rightarrow \mathbb{R}$.

2.3 SCALING T-KAM

The trainable components of the prior and inner functions are shared across the features of each input $\mathbf{x}^{(b)}$, while the outer generator functions remain separate for each output dimension. Specifically, the learnable functions are defined as:

$$\mathbf{f} = \begin{pmatrix} (f_{1,1}, \dots, f_{1,n_z}) \\ (f_{2,1}, \dots, f_{2,n_z}) \\ \vdots \\ (f_{2n_z+1,1}, \dots, f_{2n_z+1,n_z}) \end{pmatrix}, \quad \boldsymbol{\Phi} = \begin{pmatrix} (\Phi_{1,1}, \dots, \Phi_{1,2n_z+1}) \\ (\Phi_{2,1}, \dots, \Phi_{2,2n_z+1}) \\ \vdots \\ (\Phi_{n_x,1}, \dots, \Phi_{n_x,2n_z+1}) \end{pmatrix}, \quad (9)$$

where n_x denotes the dimensionality of the observed data.

From this point forward, we formulate our derivations over a multivariate probability space $(\mathcal{Z}, \mathcal{B}(\mathcal{Z}), P)$, where \mathcal{Z} no longer represents a subinterval of the real line, but rather a subspace of $\mathbb{R}^{(2n_z+1) \times n_z}$. The measure P defines a product distribution over the latent variables:

$$P(\mathbf{z} | \mathbf{f}) = \pi_{1,1} \otimes \dots \otimes \pi_{2n_z+1,n_z},$$

where each component $\pi_{j,k}$ is defined via exponential tilting, as introduced in Sec. 2.1. The full latent vector \mathbf{z} is a matrix-valued random variable composed of the independent latent features.

2.3.1 GENERATOR

The generator, \mathcal{G} , can be considered a separate generator network allowing for more flexible realizations, such as convolutional layers when adherence to Eq. 1 is not required. Deepening this generator, as guided by Liu et al. (2024) for the Kolmogorov-Arnold Network (KAN), does not replace KART as the innermost foundation of T-KAM:

$$x_o^{(s)} = \sum_{l_n=1}^{L_n} h_{o,l_n} \left(\dots h_{l_3,l_2} \left(\sum_{l_1=1}^{L_1} h_{l_2,l_1} \left(\sum_{q=1}^{2n_z+1} \Phi_{l_1,q} \left(\sum_{p=1}^{n_z} z_{q,p}^{(s)} \right) \right) \right) \right) + \epsilon_o^{(s)}. \quad (10)$$

Here, each h represents a hidden layer introduced between the outer sum of Eq. 1, and the output feature space to allow for more expressivity when required. In fact, each successive instance of h can be interpreted as a distinct outer sum of Eq. 1, where the inner sum corresponds to the previous layer. This is valid provided that:

$$L_1 = 2(2n_z + 1) + 1, \quad L_2 = 2L_1 + 1, \quad \dots \quad L_n = 2L_{n-1} + 1. \quad (11)$$

Thus, a smooth transition between the latent space and data space can be achieved by progressively doubling layer widths, eliminating the need for arbitrary choices while maintaining relaxed compliance with KART. Strict adherence to KART can be achieved for hidden layer $h_{l_k,l_{k-1}}$ by applying either a sigmoid or affine transformation after layer $h_{l_{k-2},l_{k-3}}$ to shift its range back to $[0, 1]^{L_{k-1}}$. However, using sigmoid may lead to vanishing gradients and we suggest that function domains are less critical to KART than its structural properties and should not be prioritized over maintaining gradient flow and avoiding saturation.

Adopting a KAN-based generator also allows for training with L1 regularization, followed by pruning with the method proposed by Liu et al. (2024). This enables further model compression beyond the baseline structure defined by KART.

2.3.2 MIXTURE PRIOR

As noted in Sec. 2.1, the independence of the priors $\pi_{q,p}$ limits expressivity. Moreover, the summation over p in Eq. 8 accumulates the variances of sampled $z_{q,p}$, which can lead to overly diffuse representations. To address this, particularly for more complex generative tasks such as those in Sec. 3.2, we relax the strict adherence to KART by reformulating the prior as a mixture distribution. This involves moving the summation over p out of the generator and absorbing it into the prior, yielding a mixture model:

$$\sum_{p=1}^{n_z} \pi_{q,p}(z) = \sum_{p=1}^{n_z} \alpha_{q,p} \frac{\exp(f_{q,p}(z))}{Z_{q,p}} \pi_0(z), \quad \text{where} \quad \sum_{p=1}^{n_z} \alpha_{q,p} = 1, \quad \alpha_{q,p} \geq 0. \quad (12)$$

Here, $\alpha_{q,p}$ denote mixture weights, practically enforced via a softmax function. The resulting distribution defines a mixture of energy-based priors. Sampling becomes more efficient than in the previous formulation, as it proceeds component-wise using ITS for discrete variables, (Devroye, 2006). However, this violates adherence to KART, since F now corresponds to a discrete rather than continuous CDF.

The mixture proportions are learned by replacing the log-prior in Eq. 18 with the logarithm of Eq. 12. To encourage balanced weighting and reduce model complexity, L1 regularization can be applied to $\alpha_{q,p}$ and small values can be pruned.

Component selection follows a categorical distribution over $p = 1, \dots, n_z$, determined by $\alpha_{q,p}$. Let $u_{\text{mix}} \sim \mathcal{U}(u_{\text{mix}}; 0, 1)$. Guided by Devroye (2006) regarding how ITS applied to discrete variables, the selected component p^* is given by:

$$p^* = \min \left\{ j \mid \sum_{p=1}^j \alpha_{q,p} \geq u_{\text{mix}} \right\}. \quad (13)$$

This ensures that each component p^* is selected with probability α_{q,p^*} . ITS can then be used to sample from the chosen component, (see 2.4.3).

2.3.3 DEEP KAN PRIOR

If required, the energy functions $f_{q,p}$ can be deepened using the KAN approach. In fact, each $f_{q,p}$ can itself be a realization of Eq. 1 when its domain is restricted to $[0, 1]$. This extension introduces new challenges:

1. Prior interpretability is reduced, complicating the recovery of trained priors.
2. The component-wise structure is compromised, undermining the validity of ITS and KART.

Instead, we propose removing the summation over p in Eq. 8 and reparameterizing the prior using a multilayer KAN energy function, which can be deepened as needed:

$$P(\mathbf{z} | \mathbf{f}) = \frac{1}{\mathcal{Z}} \cdot \exp \left(\sum_{q=1}^{2n_z+1} \Psi_{q,p} \left(\sum_{p=1}^{n_z} f_{q,p}(z) \right) \right) \cdot \pi_0(\mathbf{z}), \quad (14)$$

where $\mathbf{z} \in \mathcal{Z} \subset \mathbb{R}^{n_z}$, and is constrained to $[0, 1]^{n_z}$ when strict adherence to KART is required. Sampling from this prior can be carried out using the Unadjusted Langevin Algorithm (ULA), as described in Sec. 2.5.2. This is not investigated in the experiments, since it is simply equivalent to the model of Pang et al. (2020), reformulated as a KAN.

2.4 MAXIMUM LIKELIHOOD TRAINING

With N_x training examples in a batch, the optimization objective is the minimization of the negative log-marginal likelihood:

$$\min_{\mathbf{f}, \Phi} \mathcal{L}(\mathbf{x}^{(1)}, \dots, \mathbf{x}^{(N_x)}) = \min_{\mathbf{f}, \Phi} \left[- \sum_{b=1}^{N_x} \log \left(P(\mathbf{x}^{(b)} | \mathbf{f}, \Phi) \right) \right]. \quad (15)$$

The conditional dependency on the collection, \mathbf{f}, Φ , represents all learnable elements of T-KAM. For each sample of $\mathbf{x}^{(b)}$, the log-marginal likelihood in Eq. 15 can be separated out into two log-distributions by first introducing the latent vector, \mathbf{z} , otherwise absent upon marginalization over the latent distribution. This is shown under Sec. A.4.2, and the resulting expectation exhibits a lack of dependence on sampling, as proven under Sec. A.4.3:

$$\nabla_{\mathbf{f}, \Phi} \left[\log P(\mathbf{x}^{(b)} | \mathbf{f}, \Phi) \right] = \mathbb{E}_{P(\mathbf{z} | \mathbf{x}^{(b)}, \mathbf{f}, \Phi)} \left[\nabla_{\mathbf{f}} [\log P(\mathbf{z} | \mathbf{f})] + \nabla_{\Phi} \left[\log P(\mathbf{x}^{(b)} | \mathbf{z}, \Phi) \right] \right], \quad (16)$$

2.4.1 LOG-PRIOR

Given the independence of the prior’s parameters, the log-prior can be modeled as a sum over the univariate cases:

$$\log \left(P(\mathbf{z} | \mathbf{f}) \right) = \sum_{q=1}^{2n_z+1} \sum_{p=1}^{n_z} \log \left(\pi_{q,p}(z_{q,p}) \right) = \sum_{q=1}^{2n_z+1} \sum_{p=1}^{n_z} f_{q,p}(z_{q,p}) + \log \left(\pi_0(z_{q,p}) \right) - \log \left(Z_{q,p} \right) \quad (17)$$

Tractable normalization is available through Eq. 6, however it may be more efficient to discard normalization in the learning gradient. In Sec. A.4.4, we derive the contrastive divergence learning gradient for T-KAM, which is faster to train and more typical of energy-based modeling:

$$\begin{aligned} \mathbb{E}_{P(\mathbf{z} | \mathbf{x}, \mathbf{f}, \Phi)} \left[\nabla_{\mathbf{f}} [\log P(\mathbf{z} | \mathbf{f})] \right] &= \mathbb{E}_{P(\mathbf{z} | \mathbf{x}, \mathbf{f}, \Phi)} \left[\nabla_{\mathbf{f}} \sum_{q=1}^{2n_z+1} \sum_{p=1}^{n_z} f_{q,p}(z_{q,p}) \right] \\ &\quad - \mathbb{E}_{P(\mathbf{z} | \mathbf{f})} \left[\nabla_{\mathbf{f}} \sum_{q=1}^{2n_z+1} \sum_{p=1}^{n_z} f_{q,p}(z_{q,p}) \right]. \end{aligned} \quad (18)$$

Here, \mathbf{z} is sampled from $P(\mathbf{z} | \mathbf{f})$ and $P(\mathbf{z} | \mathbf{x}^{(b)}, \mathbf{f}, \Phi)$ and reflects a univariate element of the prior model. The expectation with respect to the posterior can be approximated using Importance

Sampling (IS), outlined under Secs. 2.4.4 & A.6.1, or a standard Monte Carlo estimator when using Langevin sampling methods. The prior expectation may always be approximated with a Monte Carlo estimator taken across samples:

$$\mathbb{E}_{P(z|f)} \left[\nabla_{\mathbf{f}} \sum_{q=1}^{2n_z+1} \sum_{p=1}^{n_z} f_{q,p}(z_{q,p}) \right] \approx \frac{1}{N_s} \sum_{s=1}^{N_s} \nabla_{\mathbf{f}} \sum_{q=1}^{2n_z+1} \sum_{p=1}^{n_z} f_{q,p}(z_{q,p}^{(s)}) \quad \text{where } z_{q,p}^{(s)} \sim \pi_{q,p}(z). \quad (19)$$

The gradient of Eq. 18 can therefore be viewed as a element-wise correction to the prior, incorporating information from the observations to align the prior with the posterior, thereby following the philosophy of empirical Bayes. The gradient can then be evaluated via autodifferentiation.

2.4.2 LOG-LIKELIHOOD

Depending on the task the log-likelihood can be modeled in multiple ways. For example, a Gaussian model might be adopted for images, and an autoregressive model for text. It can also be realized into a multimodal generative modeling framework using the principles outlined by Yuan et al. (2024).

$$\log \left(P \left(\mathbf{x}^{(b)} \mid \mathbf{z}, \Phi \right) \right) = \begin{cases} -\frac{\|\mathbf{x}^{(b)} - \tilde{\mathbf{x}}\|_2^2}{2\sigma_{\text{llhood}}^2} + \text{const}, & \text{(static continuous data)} \\ \sum_{o=1}^{n_x} \sum_{c=1}^K x_{o,c}^{(b)} \log \tilde{x}_{o,c} + \text{const}, & \text{(static discrete data)} \\ \sum_{t=1}^T \log \left(P \left(\mathbf{x}^{(b,t)} \mid \mathbf{x}^{(b,1)}, \dots, \mathbf{x}^{(b,t-1)}, \mathbf{z}, \Phi \right) \right), & \text{(sequential data)} \end{cases} \quad (20)$$

Here, $\tilde{\mathbf{x}}$ is a generated sample from Eq. 8 corresponding to a single batch item, $\mathbf{x}^{(b)}$, σ_{llhood} is a hyperparameter subject to assumptions regarding the variance of the data, and K denotes the number of discrete classes. The learning gradient attributed to the log-likelihood can also be evaluated using autodifferentiation, after first approximating the posterior expectation with IS or MC estimators.

The code in Sec. A.1 also provides an option to augment the first likelihood model with an additional perceptual loss term (Johnson et al., 2016) using features extracted from the pretrained VGG-16 CNN (Simonyan & Zisserman, 2015). This could have yielded higher-fidelity images for Sec. 3.2, but it was not adopted in this study due to the computational overhead of Langevin sampling.

2.4.3 PRIOR INVERSE TRANSFORM SAMPLING

In Eqs. 8 & 19, $z_{q,p}$ is drawn from $\pi_{q,p}$ with inverse transform sampling, (ITS) (Devroye, 1986). ITS can be used to sample from a component of the latent distribution, $\pi_{q,p}$, made possible given the unique characteristics of T-KAM. Specifically, the univariate, finite-grid structure of the constituent functions enables quadrature/interpolating integral approximations.

1. **CDF inversion:** Sampling occurs using the inverse cumulative distribution function (CDF): The CDF for a single component, $F_{\pi_{q,p}}$, is:

$$F_{\pi_{q,p}}(z') = \frac{\int_{z_{\min}}^{z'} \exp(f_{q,p}(z)) \pi_0(z) dz}{Z_{q,p}}, \quad Z_{q,p} = \int_{z_{\min}}^{z_{\max}} \exp(f_{q,p}(z)) \pi_0(z) dz. \quad (21)$$

These two integrals can be conveniently and efficiently approximated using Gauss-Kronrod quadrature, (Laurie, 1997), given that $f_{q,p}$ is univariate and defined on a bounded grid:

$$G(z) = \exp(f_{q,p}(z)) \pi_0(z), \quad \int_{z_{\min}}^{z'} G(z) dz \approx \sum_{i=1}^{N_{\text{quad}}} w_i G(z_i^{\text{node}}), \quad (22)$$

where z_i^{node} and w_i are the Gauss-Legendre quadrature nodes and weights for the interval $[z_{\min}, z']$. A random variable is uniformly drawn and shared across q , $u_p \sim \mathcal{U}(u_p; 0, 1)$. The first interval where $F_{\pi_{q,p}}(z)$ is greater than u_p scaled by $Z_{q,p}$ is identified:

$$k^* = \min \left\{ j \mid \sum_{i=1}^j w_i G(z_i^{\text{node}}) \geq Z_{q,p} \cdot u_p \right\}. \quad (23)$$

2. **Linear interpolation:** The sample z_p is interpolated within the subset, $[z_{k^*-1}^{\text{node}}, z_{k^*}^{\text{node}}]$:

$$z_p \approx z_{k^*-1}^{\text{node}} + (z_{k^*}^{\text{node}} - z_{k^*-1}^{\text{node}}) \cdot \frac{u_p - F_{\pi_{q,p}}(z_{k^*-1}^{\text{node}})}{F_{\pi_{q,p}}(z_{k^*}^{\text{node}}) - F_{\pi_{q,p}}(z_{k^*-1}^{\text{node}})}. \quad (24)$$

The procedure ensures an efficient, exact and unbiased generation of samples, $z_{q,p}$, distributed according to $\pi_{q,p}$. It can be vectorized to generate samples from all prior elements.

2.4.4 POSTERIOR EXPECTATIONS WITH IMPORTANCE SAMPLING

The log-marginal likelihood and its learning gradient presented in Eqs. 15 & 16, involve expectations with respect to the posterior $P(\mathbf{z} | \mathbf{x}^{(b)}, \mathbf{f}, \Phi)$, which is potentially multimodal and complex. We propose Importance Sampling (IS) (Goertzel, 1949) as an efficient method for estimating its expectation when prior task knowledge can be incorporated into the model to improve prior-posterior alignment and the quality of the IS estimator.

IS provides a quick approximation of the posterior expectation without requiring extensive exploration. In contrast, ULA, (introduced in Sec. 2.5.2) is more stochastic and exploratory, often yielding higher-quality samples from the posterior, when the prior is poorly matched.

The following procedure is elaborated in more detail under Sec. A.6.1:

1. **Proposal distribution:** N_s independent samples, $\{\mathbf{z}^{(s)}\}_{s=1}^{N_s}$, are drawn from the proposal distribution, $Q(\mathbf{z}) = P(\mathbf{z} | \mathbf{f})$, which the target distribution, $P(\mathbf{z} | \mathbf{x}^{(b)}, \mathbf{f}, \Phi)$ must be absolutely continuous with respect to. Sampling from Q is tractable with the procedure outlined in Sec. 2.4.3.

2. **Importance weights:** The normalized importance weights are evaluated:

$$w_{\text{norm}}(\mathbf{z}^{(s)}) = \frac{w(\mathbf{z}^{(s)})}{\sum_{r=1}^{N_s} w(\mathbf{z}^{(r)})} = \text{softmax}_s \left(\log(P(\mathbf{x}^{(b)} | \mathbf{z}^{(s)}, \Phi)) \right). \quad (25)$$

3. **Effective Sample Size:** To prevent weight degeneracy, resampling is conducted when the Effective Sample Size (ESS) falls below a threshold specified by a hyperparameter, γ :

$$ESS = \frac{1}{\sum_{s=1}^{N_s} w_{\text{norm}}(\mathbf{z}^{(s)})} < \gamma \cdot N_s. \quad (26)$$

Otherwise, the weights are taken without alteration, (i.e. the next step is skipped). When the weights are uniformly spread the ESS evaluates to N_s . High-variance weights with a low ESS indicate that many samples contribute minimally, resulting in inefficient sampling. Resampling focuses learning on samples that are more representative of the posterior distribution, which maximizes the usefulness of each parameter update.

4. **Resample:** If required, the population, $\{\mathbf{z}^{(s)}, w_{\text{norm}}(\mathbf{z}^{(s)})\}_{s=1}^{N_s}$, is resampled from. There are multiple ways to accomplish this, (Douc et al., 2005). Systematic, stratified, and residual resampling are provided in the codebase under Sec. A.1, parallelized on the CPU. In this study, we adopted residual resampling, (explained under Sec. A.6.2).

5. **Expectation estimation:** The posterior expectation of an arbitrary function $\rho(\mathbf{z})$, (e.g., the log-likelihood), is estimated with a Monte Carlo estimator:

$$\mathbb{E}_{P(\mathbf{z} | \mathbf{x}^{(b)}, \mathbf{f}, \Phi)}[\rho(\mathbf{z})] \approx \sum_{s=1}^{N_s} \rho(\mathbf{z}_{\text{resampled}}^{(s)}) \cdot w_{\text{norm}}(\bar{\mathbf{z}}_{\text{resampled}}^{(s)}). \quad (27)$$

This is used to estimate the log-marginal likelihood and its gradient in Eqs. 15 and 16. However, unlike ULA (discussed in Sec. 2.5.2 and demonstrated in Sec. 3.2), IS fails to support posterior exploration when the prior is poorly aligned, making it unsuitable for general-purpose tasks beyond those similar to the datasets presented in Secs. 3.1.

2.5 POPULATION-BASED AND LANGEVIN MONTE CARLO POSTERIOR SAMPLING

To mitigate the poor convergence of multimodal ULA sampling, we introduce a training criterion that facilitates posterior annealing. Details on the cyclic annealing schedule adopted in this study, along with practical guidance on hyperparameter selection, are provided in Sec. A.3.

2.5.1 THERMODYNAMIC TRAINING CRITERION

We inform our derivations using the Thermodynamic Integral. In place of the log-marginal likelihood outlined in Eq. 15, this uses the following representation derived in Sec. A.4.5:

$$\log \left(P(\mathbf{x}^{(b)} \mid \mathbf{f}, \Phi) \right) = \int_0^1 \mathbb{E}_{P(\mathbf{z} \mid \mathbf{x}^{(b)}, \mathbf{f}, \Phi, t)} \left[\log \left(P \left(\mathbf{x}^{(b)} \mid \mathbf{z}, \Phi \right) \right) \right] dt \quad (28)$$

Here, $P(\mathbf{z} \mid \mathbf{x}^{(b)}, \mathbf{f}, \Phi, t)$ has been introduced as the power posterior, which can be considered a representation of the original posterior distribution, with a likelihood tempered by a temperature parameter, t . This is introduced by Friel & Pettitt (2008) and organized for our purposes as follows:

$$P(\mathbf{z} \mid \mathbf{x}^{(b)}, \mathbf{f}, \Phi, t) = \frac{P(\mathbf{x}^{(b)} \mid \mathbf{z}, \Phi)^t \cdot P(\mathbf{z} \mid \mathbf{f})}{\mathcal{Z}_t},$$

$$\text{where } \mathcal{Z}_t = \mathbb{E}_{P(\mathbf{z} \mid \mathbf{f})} \left[P(\mathbf{x}^{(b)} \mid \mathbf{z}, \Phi)^t \right] = \int_{\mathcal{Z}} P(\mathbf{x}^{(b)} \mid \mathbf{z}, \Phi)^t dP(\mathbf{z} \mid \mathbf{f}) \quad (29)$$

Given the form of Eq. 29, setting $t = 0$ results in the power posterior distribution assuming the form of the prior distribution. As t increments, the posterior gradually adopts a shape more closely resembling the true Bayesian posterior measure. At $t = 1$, the posterior recovers its original form and converges to the original posterior distribution.

The effect of tempering is illustrated in Fig. 1, starting with a Gaussian prior that is entirely un-informed of $\mathbf{x}^{(b)}$. As t increases from 0 to 1, the contribution of the likelihood term in Eq. 29 progressively grows, ultimately leading to the posterior at $t = 1$. This final posterior can be interpreted as the prior updated by information from the samples of $\mathbf{x}^{(b)}$.

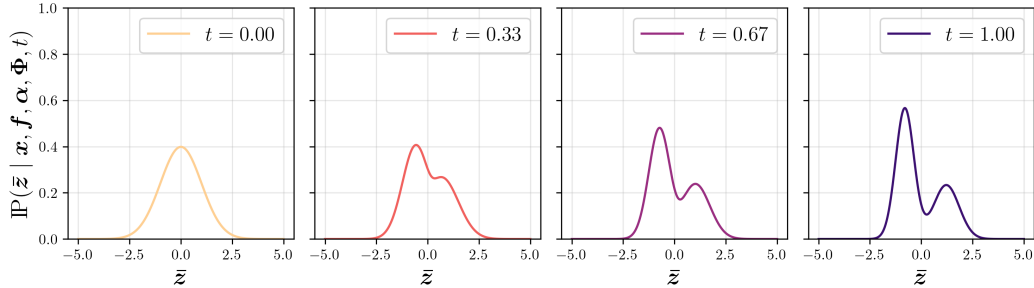


Figure 1: Demonstration of power posterior evolution with t . A simple Gaussian prior is sculpted into forms that resemble a more complex, multi-modal posterior as t is incremented from 0 to 1.

The exact calculation of the integral in Eq. 28 is feasible given that the bounds are $t = 0$, corresponding to the expectation being taken with respect to the prior, and $t = 1$, where it is taken with respect to the posterior. However, the integral can also be expressed exactly without collapsing the temperatures. This allows greater flexibility in how the integral evolves through the temperature schedule, $\{t_k\}_{k=0}^{N_t}$. In particular, the temperature schedule is discretized as:

$$\mathbf{t} = (t_0, t_1, \dots, t_{N_t}), \quad t_k \in [0, 1] \quad (30)$$

In Sec. A.4.7, the Steppingstone estimator (SE) introduced by Annis et al. (2019) is derived from the discretized Thermodynamic Integral presented by Calderhead & Girolami (2009), (and provided under Sec. A.4.6). This establishes a connection between the two, which we use to derive the learning gradient and inform our approach to the clustering the temperatures in Eq. 30:

$$\log \left(P(\mathbf{x}^{(b)} \mid \mathbf{f}, \Phi) \right) = \sum_{k=1}^{N_t} \log \left(\frac{\mathcal{Z}_{t_k}}{\mathcal{Z}_{t_{k-1}}} \right) = \sum_{k=1}^{N_t} \left(\log(\mathcal{Z}_{t_k}) - \log(\mathcal{Z}_{t_{k-1}}) \right) = \underbrace{\log(\mathcal{Z}_{t_{N_t}})}_{=\text{MLE}} - \underbrace{\log(\mathcal{Z}_{t_0})}_{=0 \text{ (Eq. 37)}}. \quad (31)$$

The log-partition ratios are estimated with Monte Carlo estimators using all annealed samples:

$$\begin{aligned} \log \left(P(\mathbf{x}^{(b)} \mid \mathbf{f}, \Phi) \right) &= \log(\mathbf{Z}_{t_{N_t}})^{\text{SS}} = \sum_{k=1}^{N_t} \log \left(\frac{\mathbf{Z}_{t_k}}{\mathbf{Z}_{t_{k-1}}} \right) \\ &\approx \frac{1}{N_s} \sum_{k=1}^{N_t-1} \sum_{s=1}^{N_s} (t_{k+1} - t_k) \left[\log P \left(\mathbf{x}^{(b)} \mid \mathbf{z}^{(s, t_k)}, \Phi \right) \right], \quad \text{where } \underbrace{\mathbf{z}^{(s, t_k)} \sim P(\mathbf{z} \mid \mathbf{x}^{(b)}, \mathbf{f}, \Phi, t_k)}_{\text{Sec.2.5.2}} \end{aligned} \quad (32)$$

SE and its variants, such as Annealed Importance Sampling (AIS) (Neal, 1998), are commonly used to estimate a model’s evidence without a tractable way to learn the prior, as they lack dependence on prior gradients beyond sampling. However, by recognizing the direct connection between the SE and MLE learning gradients, as proven in Sec. A.4.7, one can simply add the contrastive divergence learning gradient from Eq. 18 to the SE estimator.

This is valid because the SE gradient matches the MLE gradient, and the likelihood gradient is independent of the prior gradient. The posterior expectation of contrastive divergence in Eq. 18 can be estimated with a Monte Carlo estimator using the final samples of ULA.

2.5.2 UNADJUSTED LANGEVIN ALGORITHM (ULA) AND REPLICA EXCHANGE

In their implementation of Thermodynamic Integration, Calderhead & Girolami (2009) estimated the Thermodynamic Integral using the discretization in Sec. A.4.6, using population-based MCMC and Parallel Tempering (PT) (Swendsen & Wang, 1986; Marinari & Parisi, 1992; Hukushima & Nemoto, 1996) to simultaneously sample from all power posteriors.

Specifically, parallel chains were maintained at each temperature, (or Replica), using Metropolis-Hastings (MH) (Metropolis & Ulam, 1949), to drive local moves for each power posterior. They also proposed a geometric path between the prior and posterior, enabling global swaps between adjacent temperatures. This approach allowed higher temperatures to leverage the efficient mixing of lower temperatures, thereby facilitating a more thorough exploration of the posterior landscape.

We adopt a similar strategy but follow Pang et al. (2020) in using the Unadjusted Langevin Algorithm (ULA) (Rosky et al., 1978b; Brooks et al., 2011) without MH correction. Specifically, we update samples using the forward Euler-Maruyama discretization of the Langevin SDE, as detailed by Roberts & Stramer (2002), with the transition kernel described in Sec. A.6.3:

$$\mathbf{z}^{(i+1, t_k)} = \mathbf{z}^{(i, t_k)} + \eta \nabla_{\mathbf{z}^{(i, t_k)}} \log \gamma \left(\mathbf{z}^{(i, t_k)} \right) + \sqrt{2\eta} \boldsymbol{\epsilon}^{(i, t_k)}, \quad (33)$$

where η is the step size, $\boldsymbol{\epsilon}^{(i, t_k)} \sim \mathcal{N}(\mathbf{0}, \mathbf{I})$, and γ_{t_k} denotes the target power posterior:

$$\log \gamma \left(\mathbf{z}^{(i, t_k)} \right) = \log P(\mathbf{z}^{(i, t_k)} \mid \mathbf{x}^{(b)}, \mathbf{f}, \Phi, t_k) \propto t_k \log P(\mathbf{x}^{(b)} \mid \mathbf{z}^{(i, t_k)}, \Phi) + \log P(\mathbf{z}^{(i, t_k)} \mid \mathbf{f}).$$

ULA is best suited for smooth, unimodal distributions, but annealing with power posteriors can improve sampling from multimodal distributions. Mixing can be further improved by periodically swapping populations between randomly selected adjacent temperatures, subject to:

$$r = \frac{P(\mathbf{x}^{(b)} \mid \mathbf{z}^{(i, t_{k+1})}, \Phi)^{t_k} P(\mathbf{x}^{(b)} \mid \mathbf{z}^{(i, t_k)}, \Phi)^{t_{k+1}}}{P(\mathbf{x}^{(b)} \mid \mathbf{z}^{(i, t_k)}, \Phi)^{t_k} P(\mathbf{x}^{(b)} \mid \mathbf{z}^{(i, t_{k+1})}, \Phi)^{t_{k+1}}}, \quad (34)$$

where the proposed swap, $\mathbf{z}^{(i, t_{k+1})} \leftrightarrow \mathbf{z}^{(i, t_k)}$, is accepted with probability: $\min(1, r)$.

3 EXPERIMENTS

Our experiments are designed to highlight the unique advantages of T-KAM and to compare the proposed strategies for scaling and training. In Sec. 3.1, we demonstrate the effects of introducing different inductive biases through the choice of reference distributions in Eq. 4, as well as through the KAN basis functions used for $f_{q,p}$ and $\Phi_{o,q}$ with comparisons between Radial Basis Functions

(RBFs) (Li, 2024) and Fourier bases (FFTs) (Xu et al., 2024). We show that, when appropriate biases are encoded, importance sampling becomes a viable and highly efficient training strategy. We also demonstrate that the model remains effective when strictly adhering to KART with independent energy-based priors, thereby validating the use of KART as a source of structural inductive bias.

In Sec. 3.2, we evaluate the mixture EBM prior, sampled via component-wise ITS and paired with CNN-decoder architectures, which are smaller variants of those used by Pang et al. (2020). We additionally compare T-KAM trained using single-posterior ULA sampling with the MLE criterion against a population-based ULA sampling strategy using the SE criterion. These comparisons assess the practicality of using mixture distributions for scaling T-KAM and using annealing to improve training for high-dimensional RGB images.

To quantify the fidelity of generated data in a more reliable manner than previous studies in the literature, we used effectively unbiased metrics based on the principles outlined by Chong & Forsyth (2020). By applying linear regression to extrapolate the values of standard metrics to an infinitely sized sample set, Monte Carlo error was mitigated, (otherwise associated with finite sample sizes).

For Sec. 3.2, we gathered $\overline{\text{FID}}_\infty$ and $\overline{\text{KID}}_\infty$, which are effectively unbiased estimators of the Fréchet Inception Distance and Kernel Inception Distance, introduced by Heusel et al. (2018); Bińkowski et al. (2021) respectively. The set of sample sizes used for the linear regression were: 1000, 1200, 1400, 1600, 1800, 2000, 2200, 2400, 2600, 2800, 3000.

However, we recognise that quantifying the fidelity of generated data is inherently challenging and not an exact science. While the metrics used in this study have limitations, they align with those commonly found in the literature. Our conclusions are also informed by our subjective perception of the images. Furthermore, no metrics were applied in Secs. 3.1.1 & 3.1.1, as vision metrics rely on the Inception V3 model trained on ImageNet (Szegedy et al., 2015), potentially introducing bias against other datasets, especially non-RGB images.

3.1 IMPORTANCE SAMPLING

3.1.1 MNIST & FMNIST

The MNIST (Deng, 2012) and FMNIST (Xiao et al., 2017) datasets are grayscale datasets that can be modeled with the first likelihood model from Eq. 20. The first collection of benchmarks presented in Sec. A.2 were obtained using the hyperparameters and architecture specified for this experiment in Tab. 4. T-KAM was trained for 10 epochs with 50,000 training examples, an importance sample size of $N_s = 100$, and a batch size of $N_x = 100$, (corresponding to 5,000 parameter updates). Prior sampling was conducted with ITS and posterior expectations were estimated with IS. The architecture was guided by KART and independent priors were used.

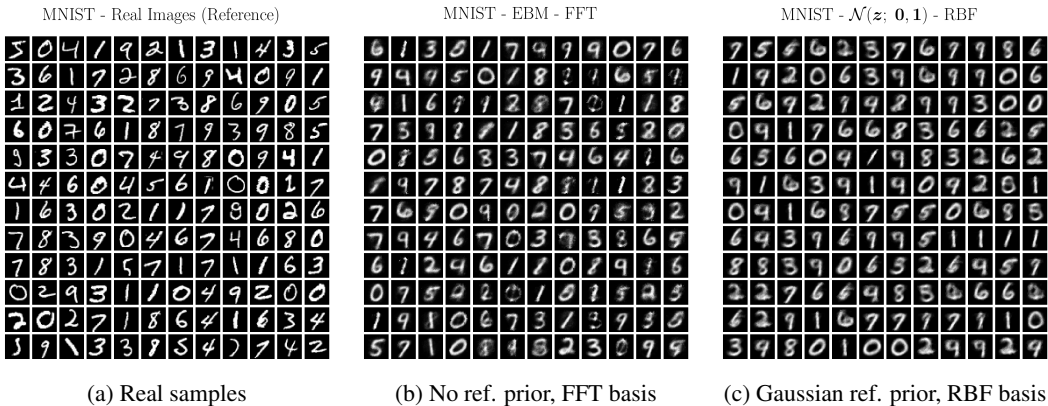


Figure 2: Generated MNIST examples using different bases and exponentially-tilted priors

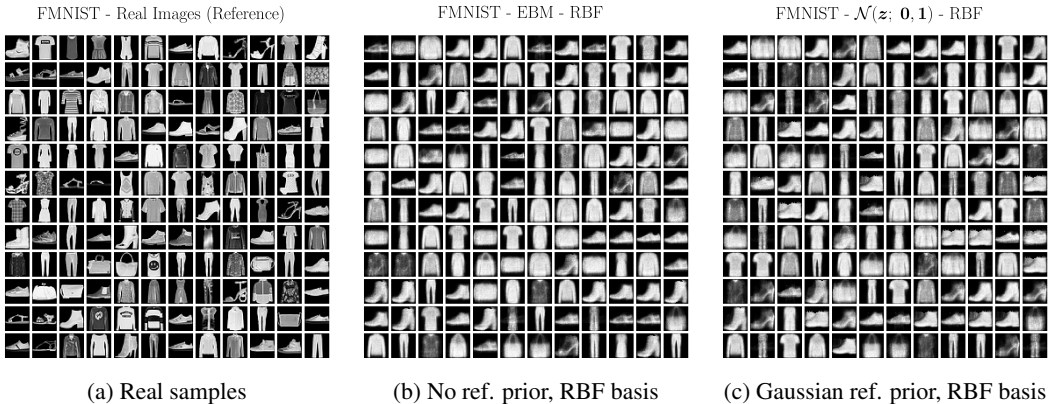


Figure 3: Generated FMNIST examples using different bases and exponentially-tilted priors

T-KAM generated a diverse set of samples when a non-restrictive reference prior was used, (Gaussian or no reference), thus validating importance sampling and independent energy-based priors for simple datasets. Subjectively, the best MNIST samples arose with no reference prior and RBF bases, whereas the best FMNIST samples came from a Gaussian reference prior with RBF bases, potentially because FMNIST has smoother features than MNIST.

The additional samples plotted in Sec. A.7.1 illustrate that the choice and combination of bases and reference priors are important. Poorly chosen combinations led to posterior collapse and low-quality samples, thereby showcasing the effect of inductive bias in guiding sample quality.

In Sec. A.8, examples of trained univariate latent distributions have been plotted to demonstrate T-KAM’s interpretability. Learning can be understood by how T-KAM reshaped its latent representation relative to the initial reference prior. For instance, lognormal priors showed little change, indicating posterior collapse, and FFTs caused much sharper relationships than the smoother RBFs.

3.1.2 2D DARCY FLOW PRESSURES

The dataset used in this experiment was sourced from Li et al. (2021). The Darcy flow equation is a second-order elliptic partial differential equation (PDE) that models various physical phenomena, including fluid flow through porous media and heat conduction. At steady state, its two-dimensional form on the unit square with Dirichlet boundary conditions is given by:

$$\begin{aligned}
 -\nabla \cdot (k(\mathbf{z}), \nabla u(\mathbf{z})) &= f(\mathbf{z}), & \mathbf{z} &\in [0, 1]^2, \\
 u(\mathbf{z}) &= 0, & \mathbf{z} &\in \partial[0, 1]^2,
 \end{aligned} \tag{35}$$

where $k(\mathbf{z})$ is the 2D permeability field, $u(\mathbf{z})$ represents the 2D pressure field, and $f(\mathbf{z})$ is a forcing function evaluated at \mathbf{z} . Generating new flow-pressure samples is a challenging task in machine learning. One approach is to use input permeability samples while employing the Fourier Neural Operator (FNO) (Li et al., 2021), to learn the solution operator mapping between permeability and flow pressure. However, in this study, we use the purely generative task to illustrate how weak inductive biases can influence what T-KAM learns.

T-KAM was trained to generate new Darcy flow pressures using a batch size and importance sample size of $N_x = 100$, $N_s = 100$, and the first likelihood model in Eq. 20. Training spanned 1,000 epochs with 1,000 training examples, resulting in 10,000 parameter updates. All other hyperparameters are provided in Tab. 5. Prior sampling was conducted with ITS and posterior expectations were estimated with IS. The architecture was guided by KART and independent priors were used.

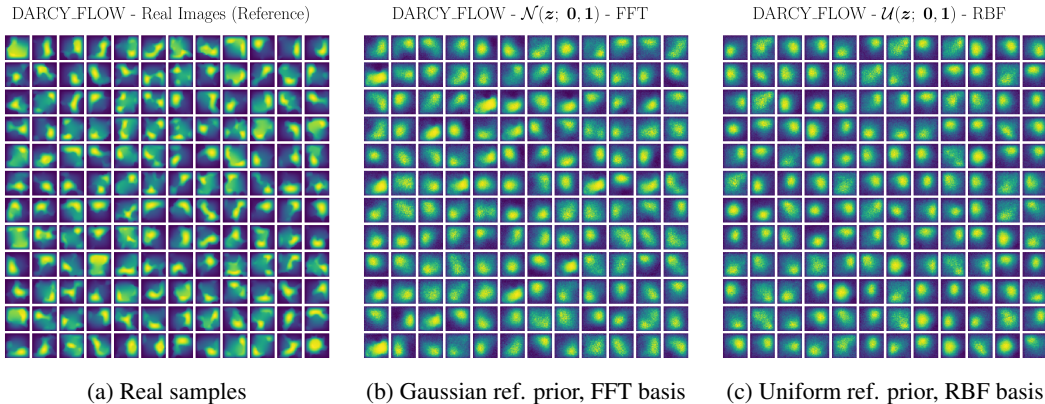


Figure 4: Generated Darcy flow examples using different bases and exponentially-tilted priors

RBFs tended to oversmooth the solution space while FFTs were more effective at capturing large-scale spatial periodicity. This likely stems from their suitability in representing periodic spatial relationships, a property that aligns well with the structure of the Darcy flow, as previously shown by the success of the FNO, which also uses Fourier methods. This is somewhat reflected by Fig. 32, which depicts some periodicity in the learned, exponentially-tilted distributions on $z_{q,p}$.

However, FFT-parameterized energy functions were also found to be non-smooth and potentially discontinuous, which is also illustrated by the distributions plotted in Fig. 32. This might have compromised adherence to KART and future work might explore incorporating regularization to improve their smoothness. Overall, the results show that the choice of basis functions serves as an additional mechanism for encoding inductive bias, complementing the role of the reference prior.

Once again, importance sampling only proved to be viable when appropriate inductive biases were encoded, and some combinations of bases and reference priors failed to learn meaningful features, (demonstrated by the extra samples of Sec. A.7.3).

3.2 LANGEVIN MONTE CARLO AND STEPPINGSTONE ESTIMATOR

T-KAM, when adherent to KART, can be interpreted as a dense or spline-based network. However, for spatial data, convolutional neural networks (CNNs) (LeCun et al., 2015), are more suitable as the generator, \mathcal{G} . In addition to their computational efficiency through weight sharing, CNNs offer a key advantage over dense networks due to their spatial inductive bias: sequences of convolutional layers implement shift-equivariant transformations that are well-suited for images.

We evaluated T-KAM using a CNN generator against two RGB image datasets at different resolutions, SVHN (32×32) (Netzer et al., 2011) and CelebA (64×64) (Liu et al., 2015). The first likelihood model in Eq. 20 was adopted for both datasets. Due to limited computational resources during this study, (detailed in Sec. A.2), training was shortened to 8,000 parameter updates, (70,000 were used in the study by Pang et al. (2020)), and smaller versions of the CNN decoders used by Pang et al. (2020) were adopted as the generator architectures.

Additionally, a single optimizer (Adam) was used to train both models, rather than using separate optimizers for the prior and generator networks. Chebyshev KAN bases (SS et al., 2024) were used for the prior energy functions, and full architectural details are provided under Sec. A.5.1.

Posterior sampling was conducted with ULA, and the standard normal reference prior was used, $\pi_0 = \mathcal{N}(z; \mathbf{0}, \mathbf{1})$. T-KAM was trained for 40 epochs with a batch size of $N_x = 100$ on 20,000 training examples. All remaining hyperparameters are provided in Tab. 6. Annealing was conducted with $N_t = 10$ power posteriors and the cyclic temperature scheduling outlined in Sec. A.3.1.

Table 1: Effectively unbiased FID and KID scores (lower is better) for SVHN (32×32).

MLE	SE
$\overline{\text{FID}}_\infty = 97.90$	$\overline{\text{FID}}_\infty = 145.64$
$\overline{\text{KID}}_\infty = 0.0827$	$\overline{\text{KID}}_\infty = 0.1407$

Table 2: Effectively unbiased FID and KID scores (lower is better) for CelebA (64×64).

MLE	SE
$\overline{\text{FID}}_\infty = 226.88$	$\overline{\text{FID}}_\infty = 209.30$
$\overline{\text{KID}}_\infty = 0.2590$	$\overline{\text{KID}}_\infty = 0.2138$

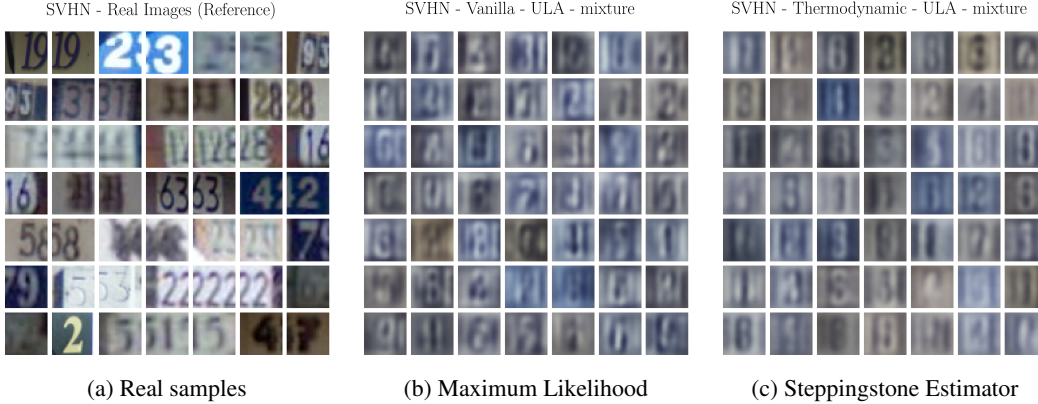


Figure 5: Generated SVHN (32×32) examples using mixture prior architecture with inverse transform sampling from the prior and Langevin sampling from the posterior

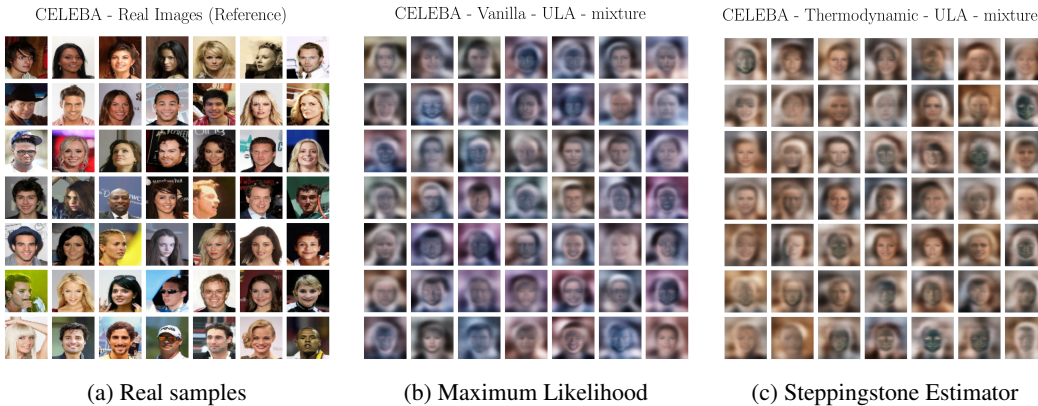


Figure 6: Generated CelebA (64×64) examples using mixture prior architecture with inverse transform sampling from the prior and Langevin sampling from the posterior

Despite being trained with reduced complexity for a small iteration count, our mixture prior model was able to generate low quality samples of SVHN and CelebA. This demonstrates the potential of component-wise ITS for exact and highly efficient sampling in replacement to the approach of Pang et al. (2020), which relied on ULA to sample from the prior, thus introducing bias and inefficiency.

SE only resulted in better image quality for CelebA and cannot be justified in this setting given its computational overhead. Alternative approaches, such as different annealing schedules or the use of autoMALA with bias correction and temperature-adaptive step size tuning, could improve performance, but they are not worth investigating until the hardware of Zetta (2024) becomes available, due to the added complexity, hyperparameter tuning, and extended training time.

4 CONCLUSIONS

T-KAM provides a principled and scalable framework for structured and informed generative modeling. Our results demonstrate that correctly chosen basis functions and reference priors can enable more efficient training on simple or well-understood datasets through importance sampling. We also show how the Kolmogorov-Arnold representation theorem can inform architectural design and introduce structural bias, allowing T-KAM’s architecture to be guided entirely by the size of its latent space. Moreover, we find that the inverse transform method offers clear advantages over Langevin Monte Carlo sampling for energy-based priors in terms of speed and exact sampling. However, the benefits of annealing and population-based MCMC remain inconclusive, suggesting directions for further work. Future investigations into the practicality of our annealing methods depend on continued hardware advancements, such as those introduced by Zetta (2024).

4.1 FUTURE WORK

4.1.1 HARDWARE ACCELERATION

Benchmarks are provided in Sec. A.2. The univariate, localized nature of spline interpolations complicates their parallelization on GPUs, since they involve sparse and recursive computations. The search operations in Eqs. 13, 23, and 69 were also difficult to parallelize on GPUs, which are generally ill-suited for search algorithms, as they often rely on conditional logic. Parallelizing conditionals can lead to thread divergence, making GPUs inefficient for these operations.

Additionally, while ITS enables fast inference and scales when the prior is a mixture model, T-KAM’s training with ULA does not scale efficiently on GPUs due to the iterative, gradient-based nature of ULA. GPUs are not well suited to Langevin Monte Carlo methods due to the irregular memory access patterns and bandwidth pressure caused by differentiating with respect to inputs, which requires storing the outputs of each layer within the generator.

Nonetheless, the unique advantages of T-KAM justify continued research and development. Moreover, Zetta (2024) introduces the Learnable Function Unit (LFU), a processor designed for efficient evaluation and differentiation of univariate, nonlinear functions in parallel, while offering precise data flow control that can mitigate the challenges of sparsity, recursion, and irregular memory access patterns. The LFU presents a promising avenue for more efficient implementations of ULA, and improved posterior sampling, potentially including bias correction and adaptive step size tuning with autoMALA, (Sec. A.6.4). Even without annealing, replacing ULA with autoMALA may yield a more robust probabilistic model with stronger theoretical guarantees.

Overall, T-KAM may prove more scalable than conventional generative models, owing to its reliance on finite representations of continuous functions and its compatibility with the LFU.

4.1.2 MORE OPPORTUNITIES FOR IMPORTANCE SAMPLING

For SVHN and CelebA, IS proved infeasible as a posterior sampler, so ULA was used for Sec. 3.2. This may be attributed to prior–posterior mismatch, which rendered the IS estimator ineffective. Moreover, relying on IS restricts the prior to its initial domain, since proposals are generated from the prior using ITS and finite-domain KAN energy functions. In contrast, ULA can explore values of z beyond this domain, enabling adaptation of the prior domain within the grid-updating scheme for KANs proposed by Liu et al. (2024).

A possible remedy for the curse of dimensionality is to learn in a reduced-order space using Principal Component Analysis (PCA) (Jolliffe & Cadima, 2016), similar to the approach of Kingma et al. (2014), who also applied PCA to train VAEs. To address prior–posterior mismatch, future work might explore how existing domain knowledge can be incorporated to shape the prior’s energy functions and align them with the posterior before training begins. Additionally, efforts should be directed toward selecting an appropriate initial domain or adapting the domain dynamically during training with IS.

4.1.3 EXPRESSIVITY

The requirements for ITS outlined in Sec. 2.1 are quite restrictive, which may limit expressivity at scale. Additionally, it is often desirable to enrich the latent space with more expressive distributions. For example, Normalizing Flows (Papamakarios et al., 2021) achieve this by applying a sequence of reversible transformations that progressively map a simple base distribution into a complex one.

This might be achievable in T-KAM by introducing more latent distributions, or revising Eq. 12 into a Mixture of Experts framework (Cai et al., 2024) where $\alpha_{q,p}$ could be realized as a more flexible kernel to enable different inductive biases. However, this might be expensive for the model by Pang et al. (2020) since its use of Langevin sampling is computationally intense. For example, the previous work of Cui & Han (2024), which divides their latent EBM space using the diffusion strategy by Ho et al. (2020), states that sampling is expensive due to their use of MCMC methods.

T-KAM could potentially circumvent the additional cost by using IS as a fast sampler, though this would require addressing its current limitations.

REFERENCES

- Jeffrey Annis, Nathan J. Evans, Brent J. Miller, and Thomas J. Palmeri. Thermodynamic integration and steppingstone sampling methods for estimating bayes factors: A tutorial. *Journal of Mathematical Psychology*, 89:67–86, April 2019. doi: 10.1016/j.jmp.2019.01.005. URL <https://osf.io/jpnb4>. Epub 2019 Feb 13.
- Leonard Bereska and Efstratios Gavves. Mechanistic interpretability for ai safety – a review, 2024. URL <https://arxiv.org/abs/2404.14082>.
- Mikołaj Bińkowski, Danica J. Sutherland, Michael Arbel, and Arthur Gretton. Demystifying mmd gans, 2021.
- Miguel Biron-Lattes, Nikola Surjanovic, Saifuddin Syed, Trevor Campbell, and Alexandre Bouchard-Côté. automala: Locally adaptive metropolis-adjusted langevin algorithm, 2024. URL <https://arxiv.org/abs/2310.16782>.
- Pakshal Bohra, Joaquim Campos, Harshit Gupta, Shayan Aziznejad, and Michael Unser. Learning activation functions in deep (spline) neural networks. *IEEE Open Journal of Signal Processing*, 1:295–309, 2020. doi: 10.1109/OJSP.2020.3039379.
- Steve Brooks, Andrew Gelman, Galin Jones, and Xiao-Li Meng. *Handbook of Markov Chain Monte Carlo*. Chapman and Hall/CRC, May 2011. ISBN 9780429138508. doi: 10.1201/b10905. URL <http://dx.doi.org/10.1201/b10905>.
- Weilin Cai, Juyong Jiang, Fan Wang, Jing Tang, Sunghun Kim, and Jiayi Huang. A survey on mixture of experts, 2024. URL <https://arxiv.org/abs/2407.06204>.
- Ben Calderhead and Mark Girolami. Estimating bayes factors via thermodynamic integration and population mcmc. *Computational Statistics & Data Analysis*, 53(12):4028–4045, 2009. ISSN 0167-9473. doi: <https://doi.org/10.1016/j.csda.2009.07.025>. URL <https://www.sciencedirect.com/science/article/pii/S0167947309002722>.
- Min Jin Chong and David Forsyth. Effectively unbiased fid and inception score and where to find them, 2020.
- Jiali Cui and Tian Han. Learning latent space hierarchical ebm diffusion models, 2024. URL <https://arxiv.org/abs/2405.13910>.
- Li Deng. The mnist database of handwritten digit images for machine learning research. *IEEE Signal Processing Magazine*, 29(6):141–142, 2012.
- Luc Devroye. *Non-Uniform Random Variate Generation*. Springer-Verlag, New York, 1986. ISBN 0-387-96305-7.

- Luc Devroye. Chapter 4 nonuniform random variate generation. In Shane G. Henderson and Barry L. Nelson (eds.), *Simulation*, volume 13 of *Handbooks in Operations Research and Management Science*, pp. 83–121. Elsevier, 2006. doi: [https://doi.org/10.1016/S0927-0507\(06\)13004-2](https://doi.org/10.1016/S0927-0507(06)13004-2). URL <https://www.sciencedirect.com/science/article/pii/S0927050706130042>.
- Randal Douc, Olivier Cappé, and Eric Moulines. Comparison of resampling schemes for particle filtering, 2005. URL <https://arxiv.org/abs/cs/0507025>.
- Simon Duane, A.D. Kennedy, Brian J. Pendleton, and Duncan Roweth. Hybrid monte carlo. *Physics Letters B*, 195(2):216–222, 1987. ISSN 0370-2693. doi: [https://doi.org/10.1016/0370-2693\(87\)91197-X](https://doi.org/10.1016/0370-2693(87)91197-X). URL <https://www.sciencedirect.com/science/article/pii/037026938791197X>.
- Paul Dupuis and Hui Wang. Importance sampling, large deviations, and differential games. *Stochastics and Stochastic Reports*, 76:481–508, 2004.
- S. Dzhenezher and A. Skopenkov. A structured proof of kolmogorov’s superposition theorem, 2022. URL <https://arxiv.org/abs/2105.00408>.
- N. Friel and A. N. Pettitt. Marginal likelihood estimation via power posteriors. *Journal of the Royal Statistical Society. Series B (Statistical Methodology)*, 70(3):589–607, 2008. ISSN 13697412, 14679868. URL <http://www.jstor.org/stable/20203843>.
- Hao Fu, Chunyuan Li, Xiaodong Liu, Jianfeng Gao, Asli Celikyilmaz, and Lawrence Carin. Cyclical annealing schedule: A simple approach to mitigating kl vanishing, 2019. URL <https://arxiv.org/abs/1903.10145>.
- Alexander B. Givental, Boris A. Khesin, Jerrold E. Marsden, Alexander N. Varchenko, Victor A. Vassiliev, Oleg Ya. Viro, and Vladimir M. Zakalyukin (eds.). *On the representation of functions of several variables as a superposition of functions of a smaller number of variables*, pp. 25–46. Springer Berlin Heidelberg, Berlin, Heidelberg, 2009. ISBN 978-3-642-01742-1. doi: 10.1007/978-3-642-01742-1_5. URL https://doi.org/10.1007/978-3-642-01742-1_5.
- Gerald Goertzel. Quota sampling and importance functions in stochastic solution of particle problems. Technical Report AECD-2793, U.S. Atomic Energy Commission, 1949. Technical Report, June 21, 1949.
- Ian J. Goodfellow, Jean Pouget-Abadie, Mehdi Mirza, Bing Xu, David Warde-Farley, Sherjil Ozair, Aaron Courville, and Yoshua Bengio. Generative adversarial networks, 2014. URL <https://arxiv.org/abs/1406.2661>.
- Martin Hairer, Andrew M. Stuart, and Sebastian J. Vollmer. Spectral gaps for a metropolis–hastings algorithm in infinite dimensions. *The Annals of Applied Probability*, 24(6), December 2014. ISSN 1050-5164. doi: 10.1214/13-aap982. URL <http://dx.doi.org/10.1214/13-AAP982>.
- W. K. Hastings. Monte carlo sampling methods using markov chains and their applications. *Biometrika*, 57(1):97–109, 04 1970. ISSN 0006-3444. doi: 10.1093/biomet/57.1.97. URL <https://doi.org/10.1093/biomet/57.1.97>.
- Martin Heusel, Hubert Ramsauer, Thomas Unterthiner, Bernhard Nessler, and Sepp Hochreiter. Gans trained by a two time-scale update rule converge to a local nash equilibrium, 2018.
- Jonathan Ho, Ajay Jain, and Pieter Abbeel. Denoising diffusion probabilistic models, 2020. URL <https://arxiv.org/abs/2006.11239>.
- Koji Hukushima and Koji Nemoto. Exchange monte carlo method and application to spin glass simulations. *Journal of the Physical Society of Japan*, 65(6):1604–1608, June 1996. ISSN 1347-4073. doi: 10.1143/jpsj.65.1604. URL <http://dx.doi.org/10.1143/JPSJ.65.1604>.
- Justin Johnson, Alexandre Alahi, and Li Fei-Fei. Perceptual losses for real-time style transfer and super-resolution, 2016. URL <https://arxiv.org/abs/1603.08155>.

- Ian T. Jolliffe and Jorge Cadima. Principal component analysis: a review and recent developments. *Philosophical Transactions of the Royal Society A: Mathematical, Physical and Engineering Sciences*, 374(2065):20150202, 2016. ISSN 1364-503X. doi: 10.1098/rsta.2015.0202.
- JuliaCI. Benchmarktools.jl, 2024. URL <https://juliaci.github.io/BenchmarkTools.jl/stable/>. Accessed on August 20, 2024.
- George Em Karniadakis, Ioannis G. Kevrekidis, Lu Lu, Paris Perdikaris, Sifan Wang, and Liu Yang. Physics-informed machine learning. *Nature Reviews Physics*, 3(6):422–440, 2021. ISSN 2522-5820. doi: 10.1038/s42254-021-00314-5. URL <https://doi.org/10.1038/s42254-021-00314-5>.
- Diederik P. Kingma and Max Welling. Auto-encoding variational bayes, 2022. URL <https://arxiv.org/abs/1312.6114>. arXiv:1312.6114.
- Diederik P. Kingma, Danilo J. Rezende, Shakir Mohamed, and Max Welling. Semi-supervised learning with deep generative models, 2014. URL <https://arxiv.org/abs/1406.5298>.
- T. Kloek and H. K. van Dijk. Bayesian estimates of equation system parameters: An application of integration by monte carlo. *Econometrica*, 46(1):1–19, 1978. ISSN 00129682, 14680262. URL <http://www.jstor.org/stable/1913641>.
- Deqian Kong, Bo Pang, and Ying Nian Wu. Unsupervised meta-learning via latent space energy-based model of symbol vector coupling. In *Fifth Workshop on Meta-Learning at the Conference on Neural Information Processing Systems*, 2021. URL <https://openreview.net/forum?id=-pLftu7EpXz>.
- R. Larson and B.H. Edwards. *Calculus of a Single Variable*. Cengage Learning, 2008. ISBN 9780547209982. URL https://books.google.co.uk/books?id=gR7nGg5_9xcC.
- Dirk Laurie. Calculation of gauss-kronrod quadrature rules. *Math. Comput.*, 66:1133–1145, 07 1997. doi: 10.1090/S0025-5718-97-00861-2.
- Yann LeCun, Yoshua Bengio, and Geoffrey Hinton. Deep learning. *Nature*, 521(7553):436–444, May 28 2015. ISSN 1476-4687. doi: 10.1038/nature14539.
- Ziyao Li. Kolmogorov-arnold networks are radial basis function networks, 2024. URL <https://arxiv.org/abs/2405.06721>.
- Zongyi Li, Nikola Kovachki, Kamyar Aizzadenesheli, Burigede Liu, Kaushik Bhattacharya, Andrew Stuart, and Anima Anandkumar. Fourier neural operator for parametric partial differential equations, 2021. URL <https://arxiv.org/abs/2010.08895>.
- Ziming Liu, Yixuan Wang, Sachin Vaidya, Fabian Ruelle, James Halverson, Marin Soljačić, Thomas Y. Hou, and Max Tegmark. Kan: Kolmogorov-arnold networks, 2024. URL <https://arxiv.org/abs/2404.19756>.
- Ziwei Liu, Ping Luo, Xiaogang Wang, and Xiaoou Tang. Deep learning face attributes in the wild, 2015. URL <https://arxiv.org/abs/1411.7766>.
- E. Marinari and G. Parisi. Simulated tempering: A new monte carlo scheme. *Europhysics Letters*, 19(6):451, jul 1992. doi: 10.1209/0295-5075/19/6/002. URL <https://dx.doi.org/10.1209/0295-5075/19/6/002>.
- Nicholas Metropolis and S. Ulam. The monte carlo method. *Journal of the American Statistical Association*, 44(247):335–341, 1949. ISSN 01621459, 1537274X. URL <http://www.jstor.org/stable/2280232>.
- Fionn Murtagh. Multilayer perceptrons for classification and regression. *Neurocomputing*, 2(5):183–197, 1991. ISSN 0925-2312. doi: [https://doi.org/10.1016/0925-2312\(91\)90023-5](https://doi.org/10.1016/0925-2312(91)90023-5). URL <https://www.sciencedirect.com/science/article/pii/0925231291900235>.

- Radford M. Neal. Annealed importance sampling, 1998. URL <https://arxiv.org/abs/physics/9803008>.
- Yuval Netzer, Tao Wang, Adam Coates, Alessandro Bissacco, Bo Wu, and Andrew Y. Ng. Reading digits in natural images with unsupervised feature learning. In *NIPS Workshop on Deep Learning and Unsupervised Feature Learning 2011*, 2011. URL http://ufldl.stanford.edu/housenumbers/nips2011_housenumbers.pdf.
- Erik Nijkamp, Mitch Hill, Tian Han, Song-Chun Zhu, and Ying Nian Wu. On the anatomy of mcmc-based maximum likelihood learning of energy-based models, 2019a. URL <https://arxiv.org/abs/1903.12370>.
- Erik Nijkamp, Mitch Hill, Song-Chun Zhu, and Ying Nian Wu. Learning non-convergent non-persistent short-run mcmc toward energy-based model, 2019b. URL <https://arxiv.org/abs/1904.09770>.
- Bo Pang, Tian Han, Erik Nijkamp, Song-Chun Zhu, and Ying Nian Wu. Learning latent space energy-based prior model, 2020. URL <https://arxiv.org/abs/2006.08205>.
- George Papamakarios, Eric Nalisnick, Danilo Jimenez Rezende, Shakir Mohamed, and Balaji Lakshminarayanan. Normalizing flows for probabilistic modeling and inference, 2021. URL <https://arxiv.org/abs/1912.02762>.
- T. Poggio and F. Girosi. Networks for approximation and learning. *Proceedings of the IEEE*, 78(9):1481–1497, 1990. doi: 10.1109/5.58326. URL <https://doi.org/10.1109/5.58326>.
- G. O. Roberts and O. Stramer. Langevin diffusions and metropolis-hastings algorithms. *Methodology and Computing in Applied Probability*, 4(4):337–357, 2002. ISSN 1573-7713. doi: 10.1023/A:1023562417138. URL <https://doi.org/10.1023/A:1023562417138>.
- P. J. Rossky, J. D. Doll, and H. L. Friedman. Brownian dynamics as smart monte carlo simulation. *The Journal of Chemical Physics*, 69(10):4628–4633, 11 1978a. ISSN 0021-9606. doi: 10.1063/1.436415. URL <https://doi.org/10.1063/1.436415>.
- P. J. Rossky, J. D. Doll, and H. L. Friedman. Brownian dynamics as smart monte carlo simulation. *The Journal of Chemical Physics*, 69(10):4628–4633, 1978b. doi: 10.1063/1.436415.
- Karen Simonyan and Andrew Zisserman. Very deep convolutional networks for large-scale image recognition, 2015. URL <https://arxiv.org/abs/1409.1556>.
- Sidharth SS, Keerthana AR, Gokul R, and Anas KP. Chebyshev polynomial-based kolmogorov-arnold networks: An efficient architecture for nonlinear function approximation, 2024. URL <https://arxiv.org/abs/2405.07200>.
- Robert Swendsen and Jian-Sheng Wang. Replica monte carlo simulation of spin-glasses. *Physical review letters*, 57:2607–2609, 12 1986. doi: 10.1103/PhysRevLett.57.2607.
- Christian Szegedy, Vincent Vanhoucke, Sergey Ioffe, Jonathon Shlens, and Zbigniew Wojna. Rethinking the inception architecture for computer vision, 2015.
- Joshua Wilkie. Numerical methods for stochastic differential equations. *Physical Review E*, 70(1), July 2004. ISSN 1550-2376. doi: 10.1103/physreve.70.017701. URL <http://dx.doi.org/10.1103/PhysRevE.70.017701>.
- Han Xiao, Kashif Rasul, and Roland Vollgraf. Fashion-mnist: a novel image dataset for benchmarking machine learning algorithms, 2017. URL <https://arxiv.org/abs/1708.07747>.
- Jinfeng Xu, Zheyu Chen, Jinze Li, Shuo Yang, Wei Wang, Xiping Hu, and Edith C. H. Ngai. Fourierkan-gcf: Fourier kolmogorov-arnold network – an effective and efficient feature transformation for graph collaborative filtering, 2024. URL <https://arxiv.org/abs/2406.01034>.
- Shiyu Yuan, Jiali Cui, Hanao Li, and Tian Han. Learning multimodal latent generative models with energy-based prior, 2024. URL <https://arxiv.org/abs/2409.19862>.

Zetta. Zetta, the next paradigm of sustainable computing. <https://zsc.ai/litepaper>, August 2024. The Zettascale Computing Corp. introduce a polymorphic computing chip technology, achieving up to 27.6x efficiency gains over the H100 GPUs through dynamically reconfigurable hardware that adapts to diverse AI models via software configuration.

Xinwei Zhang, Zhiqiang Tan, and Zhijian Ou. Persistently trained, diffusion-assisted energy-based models, 2023. URL <https://arxiv.org/abs/2304.10707>.

Song Chun Zhu and D. Mumford. Grade: Gibbs reaction and diffusion equations. In *Sixth International Conference on Computer Vision (IEEE Cat. No.98CH36271)*, pp. 847–854, 1998. doi: 10.1109/ICCV.1998.710816.

A APPENDIX

A.1 CODEBASE

The study was implemented at <https://github.com/thezettascale/T-KAM>.

A.2 COMPUTATIONAL BENCHMARKS

These benchmarks were collected for FP32 on a GPU (NVIDIA GeForce RTX 4060) with Julia’s BenchmarkTools package, (JuliaCI, 2024). The index search operations in Eqs. 23, 13, & 69 were parallelized across 20 threads on a CPU (i9-13900H @ 5.40GHz).

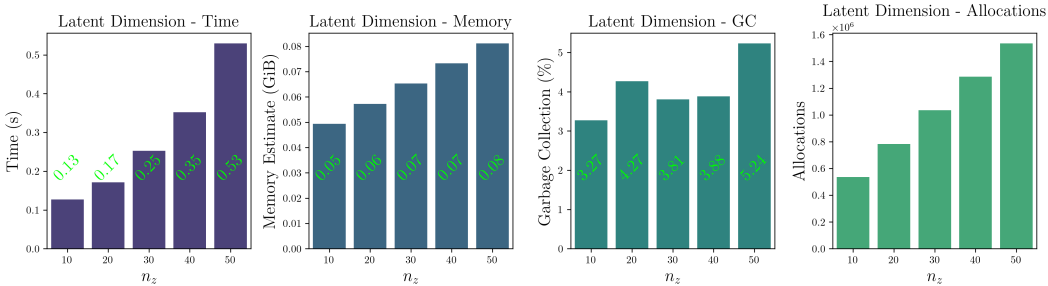


Figure 7: Benchmarks for varying latent dimensions, n_z , while sampling from independent EBM priors with ITS and estimating posterior expectations with IS. The prior had an input size of n_z and an output size of $2n_z + 1$. The generator received inputs of size $2n_z + 1$, with a hidden size of $4n_z + 2$ and an output size of 28×28 . All other hyperparameters were consistent with Tab. 4 (RBF bases). They reflect the performance of a reverse autodifferentiation of the MLE criterion, Eq. 16.

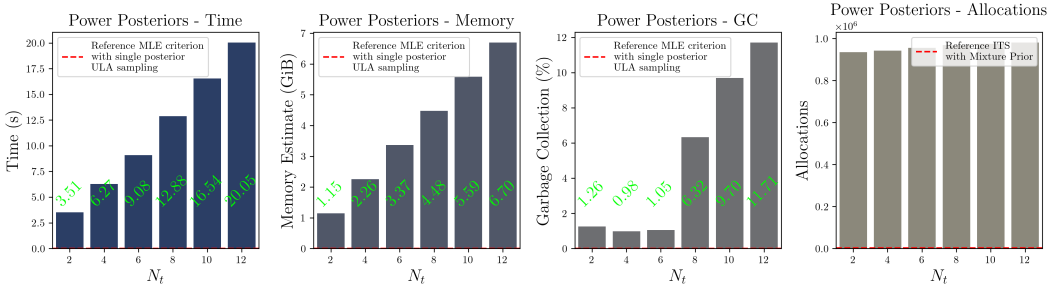


Figure 8: Benchmarks for varying amounts of temperatures, N_t , using a mixture of EBM priors (Tab. 7) with ITS sampling. Posterior expectations were estimated with SE and population-based ULA. All other hyperparameters were kept consistent with Tab. 6 (Celeb-A). They reflect the computational cost of performing a single reverse autodifferentiation of the SE criterion, Eq. 31.

A.3 GUIDANCE ON TEMPERING

A.3.1 CYCLIC ANNEALING

Calderhead & Girolami (2009) demonstrated that uniformly scheduling the discretized temperatures in Eq. 30 results in unequal contributions of adjacent power posteriors to the Thermodynamic Integral. The success of TI and SE, relies on selecting each t_k to ensure sufficient overlap of adjacent power posteriors. This overlap ensures similarity between adjacent power posteriors, as introduced in Sec. A.6.1, which influences the Monte Carlo estimator in Eq. 32, given that SE is an application of importance sampling, (Annis et al., 2019).

This overlap is quantified by the KL divergence term in Eq. 51. Maintaining small KL divergences between adjacent power posteriors can be achieved by clustering temperatures in regions where $P(\mathbf{z} | \mathbf{x}^{(b)}, \mathbf{f}, \Phi, t_k)$ changes rapidly. To accomplish this, we follow Calderhead & Girolami (2009) in adopting a power-law relationship to schedule the temperatures of Eq. 30:

$$t_k = \left(\frac{k}{N_t}\right)^p, \quad k = 0, 1, \dots, N_t, \quad (36)$$

The effect of varying p on the schedule between 0 and 1 is visualized in Fig. 9. When $p > 1$, spacing becomes denser near $t = 0$, while $p < 1$ creates denser spacing near $t = 1$. The impact of varying p on the discretized Thermodynamic Integral of Eq. 51 is illustrated in Fig. 10. The plots demonstrate that for $p > 1$, the trapezoidal bins are clustered closer to $t = 0$, concentrating the discrete approximation error towards $t = 1$.

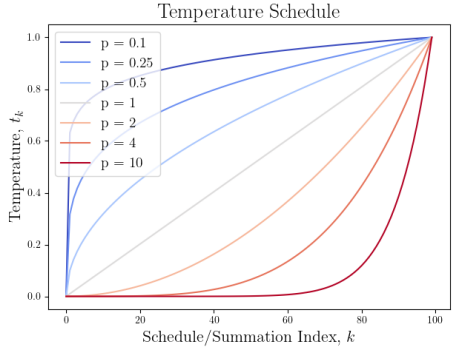
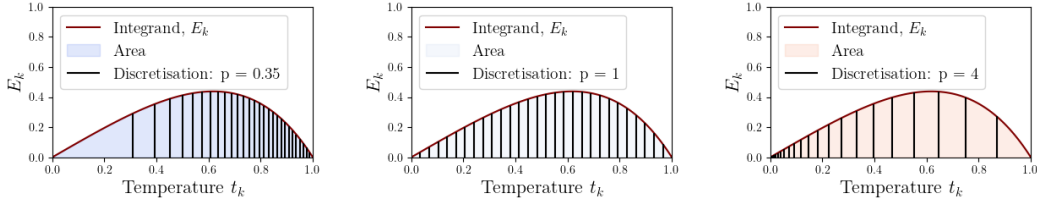


Figure 9: Power-law schedule.



(a) $p = 0.35$ schedule has more bins clustered towards $t = 1$. (b) $p = 1$ schedule is uniformly distributed between the bounds. (c) $p = 4$ schedule has more bins clustered towards $t = 0$.

Figure 10: Effect of power-law schedule clusters on integral approximation error. Evaluation points can be skewed towards a particular bound by choosing p . Increasing p provides more tempering, concentrating more evaluation points on smoother likelihoods. Tempering helps to mitigate practical challenges associated with the non-smoothness of the univariate functions in Eq. 1.

The study by Calderhead & Girolami (2009) derives an analytic term for an optimal tempering distribution in the context of linear regression models, where the power posterior in Eq. 29 is used to evaluate the plausibility of model parameters in relation to the data, rather than reflecting a latent variable posterior. However, their findings may not hold in the context of T-KAM and generative modeling, making p and the temperature schedule difficult variables to tune.

Instead, we schedule p sinusoidally across all training parameter updates, starting with a higher value of p and ending with a lower value, treated as tunable hyperparameters.

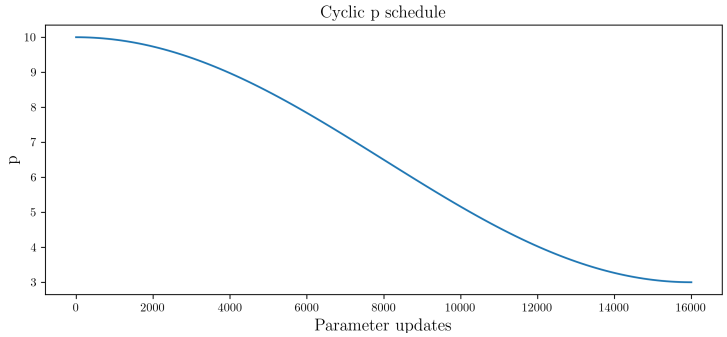


Figure 11: Cosine p schedule, decreasing from 10 to 1

Initializing $p > 1$ focuses learning on smoother likelihoods during the early stages of the cycle, where global features emerge between adjacent power posteriors. As training progresses, T-KAM will have learned the global features sufficiently well, reducing the change of measure between adjacent power posteriors of a $p > 1$ schedule. At this stage, $p(i)$ will have transitioned to $p \leq 1$, thereby shifting T-KAM’s focus towards capturing more detailed features of the posterior landscape, where training is expected to enhance its ability to generate finer details.

Guidance on selecting optimal values for the tempering hyperparameters is provided in Tab. 3.

A.3.2 CHOOSING HYPERPARAMETERS

Table 3: Tempering hyperparameters.

Hyperparameter	Description
$N_t > 1$	Specifies the number of power posteriors, enabling a smooth transition between the prior and posterior. Increasing this improves exploration but also increases cost due to the need for more MALA iterations. Typically, this is memory-bound and guided by hardware availability, such as $N_t = 5$.
$N_{\text{local}} > 1$	Determines the number of ULA or autoMALA iterations per power posterior. Although increasing this value improves the quality of samples at each stage, it also raises the computational cost, much like N_t . It can be kept at a small value, such as $N_{\text{local}} = 40$, (based on the recommendations of Nijkamp et al. (2019b;a) regarding short-run Markov chain Monte Carlo).
$N_{\text{unadjusted}} > 1$	Controls the number of autoMALA iterations performed without MH adjustments, reflecting the level of exploration at each power posterior. This can be set to 1, as guided by Biron-Lattes et al. (2024).
$p_{\text{init}} > 1, p_{\text{end}} \leq 1, N_{\text{cycles}} > 0$	Controls the evolution of tempering during training. If the data is expected to have smooth relationships, reduce both p_{init} and p_{end} . For data with finer details, increase both values to allow for better focus on capturing intricate features. Recommended values are $p_{\text{init}} = 10$, and $p_{\text{end}} = 3$, since our experience suggests that power posteriors change rapidly closer to the prior. The number of cycles, N_{cycles} , controls the periodicity of cosine scheduling similar to cyclic annealing (Fu et al., 2019).

A.4 DERIVATIONS AND OTHER IDENTITIES

A.4.1 USEFUL PROOF

The following short proof for a learning gradient with respect to an arbitrary set of parameters, θ , proves useful for other derivations in this study:

$$\begin{aligned} \mathbb{E}_{P(\mathbf{x}|\theta)} [\nabla_{\theta} \log P(\mathbf{x} | \theta)] &= \mathbb{E}_{P(\mathbf{x}|\theta)} \left[\frac{\nabla_{\theta} P(\mathbf{x} | \theta)}{P(\mathbf{x} | \theta)} \right] = \int_{\mathcal{X}} \frac{\nabla_{\theta} P(\mathbf{x} | \theta)}{P(\mathbf{x} | \theta)} dP(\mathbf{x} | \theta) \\ &= \int_{\mathcal{X}} \nabla_{\theta} P(\mathbf{x} | \theta) d\mathbf{x} = \nabla_{\theta} \int_{\mathcal{X}} P(\mathbf{x} | \theta) d\mathbf{x} = \nabla_{\theta} 1 = 0. \end{aligned} \quad (37)$$

A.4.2 MARGINAL LIKELIHOOD

$$\begin{aligned} \log \left(P(\mathbf{x}^{(b)} | \mathbf{f}, \Phi) \right) &= \mathbb{E}_{P(\mathbf{z}|\mathbf{x}^{(b)}, \mathbf{f}, \Phi)} \left[\log \left(P(\mathbf{x}^{(b)}, \mathbf{z} | \mathbf{f}, \Phi) \right) \right] \\ &= \mathbb{E}_{P(\mathbf{z}|\mathbf{x}^{(b)}, \mathbf{f}, \Phi)} \left[\log \left(P(\mathbf{z} | \mathbf{f}) \cdot P(\mathbf{x}^{(b)} | \mathbf{z}, \Phi) \right) \right] \\ &= \mathbb{E}_{P(\mathbf{z}|\mathbf{x}^{(b)}, \mathbf{f}, \Phi)} \left[\log (P(\mathbf{z} | \mathbf{f})) + \log \left(P(\mathbf{x}^{(b)} | \mathbf{z}, \Phi) \right) \right]. \end{aligned} \quad (38)$$

A.4.3 MAXIMUM LIKELIHOOD LEARNING GRADIENT

This proof demonstrates that the learning gradient with respect to an arbitrary set of parameters, θ , is independent of sampling:

$$\begin{aligned} \mathbb{E}_{P(\mathbf{z}|\mathbf{x})} [\nabla_{\theta} \log P(\mathbf{x}, \mathbf{z})] &= \mathbb{E}_{P(\mathbf{z}|\mathbf{x})} [\nabla_{\theta} \log P(\mathbf{z} | \mathbf{x}) + \nabla_{\theta} \log P(\mathbf{x})] \\ &= \mathbb{E}_{P(\mathbf{z}|\mathbf{x})} [\nabla_{\theta} \log P(\mathbf{z} | \mathbf{x})] + \mathbb{E}_{P(\mathbf{z}|\mathbf{x})} [\nabla_{\theta} \log P(\mathbf{x})] \\ &= 0 + \nabla_{\theta} \log P(\mathbf{x}), \end{aligned} \quad (39)$$

where Eq. 37 has been used to zero the expected posterior. This allows gradient flow to be disregarded in sampling procedures as shown in Eq. 16.

A.4.4 CONTRASTIVE DIVERGENCE LEARNING GRADIENT FOR LOG-PRIOR

The learning gradient attributed to the prior can be derived into a contrastive divergence framework, which is more typical of energy-based modeling literature. The prior model is solely dependent on \mathbf{f} in Eq. 4. We can rewrite Eq. 17 as:

$$\nabla_{\mathbf{f}} \log (P(\mathbf{z} | \mathbf{f})) = \nabla_{\mathbf{f}} \sum_{q=1}^{2n_z+1} \sum_{p=1}^{n_z} \log (\pi_{q,p}(z_{q,p})) = \nabla_{\mathbf{f}} \sum_{q=1}^{2n_z+1} \sum_{p=1}^{n_z} f_{q,p}(z_{q,p}) + \log (\pi_0(z_{q,p})) - \log (Z_{q,p}) \quad (40)$$

where $Z_{q,p} = \int_{\mathcal{Z}} \exp(f_{q,p}(z_p)) d\pi_0(z_p)$ is the normalization constant. We can simplify the constant using Eq. 37:

$$\begin{aligned} \mathbb{E}_{P(\mathbf{z}|\mathbf{f})} \left[\nabla_{\mathbf{f}} \log P(\mathbf{z} | \mathbf{f}) \right] &= \mathbb{E}_{P(\mathbf{z}|\mathbf{f})} \left[\nabla_{\mathbf{f}} \sum_{q=1}^{2n_z+1} \sum_{p=1}^{n_z} f_{q,p}(z_{q,p}) + \log (\pi_0(z_{q,p})) - \log (Z_{q,p}) \right] = 0 \\ &= \mathbb{E}_{P(\mathbf{z}|\mathbf{f})} \left[\nabla_{\mathbf{f}} \sum_{q=1}^{2n_z+1} \sum_{p=1}^{n_z} f_{q,p}(z_{q,p}) \right] - \nabla_{\mathbf{f}} \sum_{q=1}^{2n_z+1} \sum_{p=1}^{n_z} \log (Z_{q,p}) = 0 \\ \therefore \nabla_{\mathbf{f}} \sum_{q=1}^{2n_z+1} \sum_{p=1}^{n_z} \log (Z_{q,p}) &= \mathbb{E}_{P(\mathbf{z}|\mathbf{f})} \left[\nabla_{\mathbf{f}} \sum_{q=1}^{2n_z+1} \sum_{p=1}^{n_z} f_{q,p}(z_{q,p}) \right] \end{aligned} \quad (41)$$

Therefore the log-prior gradient of Eq. 40 can be evaluated without quadrature normalization as:

$$\nabla_{\mathbf{f}} \log P(\mathbf{z} | \mathbf{f}) = \nabla_{\mathbf{f}} \sum_{q=1}^{2n_z+1} \sum_{p=1}^{n_z} f_{q,p}(z_{q,p}) - \mathbb{E}_{P(\mathbf{z}|\mathbf{f})} \left[\nabla_{\mathbf{f}} \sum_{q=1}^{2n_z+1} \sum_{p=1}^{n_z} f_{q,p}(z_{q,p}) \right], \quad (42)$$

and the learning gradient attributed to the prior is finalized into a contrastive divergence format:

$$\begin{aligned} \mathbb{E}_{P(\mathbf{z}|\mathbf{x},\mathbf{f},\Phi)} \left[\nabla_{\mathbf{f}} [\log P(\mathbf{z} | \mathbf{f})] \right] &= \mathbb{E}_{P(\mathbf{z}|\mathbf{x},\mathbf{f},\Phi)} \left[\nabla_{\mathbf{f}} \sum_{q=1}^{2n_z+1} \sum_{p=1}^{n_z} f_{q,p}(z_{q,p}) \right] \\ &\quad - \mathbb{E}_{P(\mathbf{z}|\mathbf{f})} \left[\nabla_{\mathbf{f}} \sum_{q=1}^{2n_z+1} \sum_{p=1}^{n_z} f_{q,p}(z_{q,p}) \right]. \end{aligned} \quad (43)$$

A.4.5 DERIVING THE THERMODYNAMIC INTEGRAL

Starting from the power posterior:

$$P(\mathbf{z} | \mathbf{x}^{(b)}, \mathbf{f}, \Phi, t) = \frac{P(\mathbf{x}^{(b)} | \mathbf{z}, \Phi)^t P(\mathbf{z} | \mathbf{f})}{\mathbf{Z}_t} \quad (44)$$

The partition function \mathbf{Z}_t is given by:

$$\mathbf{Z}_t = \mathbb{E}_{P(\mathbf{z}|\mathbf{f})} \left[P(\mathbf{x}^{(b)} | \mathbf{z}, \Phi)^t \right] \quad (45)$$

Now, differentiating the log-partition function with respect to t :

$$\begin{aligned} \frac{\partial}{\partial t} \log(\mathbf{Z}_t) &= \frac{1}{\mathbf{Z}_t} \frac{\partial}{\partial t} \mathbf{Z}_t = \frac{1}{\mathbf{Z}_t} \mathbb{E}_{P(\mathbf{z}|\mathbf{f})} \left[\frac{\partial}{\partial t} P(\mathbf{x}^{(b)} | \mathbf{z}, \Phi)^t \right] \\ &= \frac{1}{\mathbf{Z}_t} \mathbb{E}_{P(\mathbf{z}|\mathbf{f})} \left[\log P(\mathbf{x}^{(b)} | \mathbf{z}, \Phi) \cdot P(\mathbf{x}^{(b)} | \mathbf{z}, \Phi)^t \right] \\ &= \mathbb{E}_{P(\mathbf{z}|\mathbf{x}^{(b)},\mathbf{f},\Phi,t)} \left[\log P(\mathbf{x}^{(b)} | \mathbf{z}, \Phi) \right] \end{aligned} \quad (46)$$

Integrating both sides from 0 to 1:

$$\int_0^1 \frac{\partial}{\partial t} \log(\mathbf{Z}_t) dt = \int_0^1 \mathbb{E}_{P(\mathbf{z}|\mathbf{x}^{(b)},\mathbf{f},\Phi,t)} \left[\log P(\mathbf{x}^{(b)} | \mathbf{z}, \Phi) \right] dt \quad (47)$$

Using the fundamental theorem of calculus, (Larson & Edwards, 2008):

$$\int_0^1 \frac{\partial}{\partial t} \log(\mathbf{Z}_t) dt = \log(\mathbf{Z}_{t=1}) - \log(\mathbf{Z}_{t=0}) = \int_0^1 \mathbb{E}_{P(\mathbf{z}|\mathbf{x}^{(b)},\mathbf{f},\Phi,t)} \left[\log P(\mathbf{x}^{(b)} | \mathbf{z}, \Phi) \right] dt \quad (48)$$

The limits of the integrals can be expressed as:

$$\begin{aligned} \log(\mathbf{Z}_{t=0}) &= \log \left(\mathbb{E}_{P(\mathbf{z}|\mathbf{f})} \left[P(\mathbf{x}^{(b)} | \mathbf{z}, \Phi)^0 \right] \right) = \log(1) = 0 \\ \log(\mathbf{Z}_{t=1}) &= \log \left(\mathbb{E}_{P(\mathbf{z}|\mathbf{x}^{(b)},\mathbf{f},\Phi)} \left[\log P(\mathbf{x}^{(b)} | \mathbf{z}, \Phi) \right] \right) = \log P(\mathbf{x}^{(b)} | \mathbf{f}, \Phi) \end{aligned} \quad (49)$$

Therefore, we obtain the log-marginal likelihood expressed as the Thermodynamic Integral:

$$\log(\mathbf{Z}_{t=1}) - \log(\mathbf{Z}_{t=0}) = \log P(\mathbf{x}^{(b)} | \mathbf{f}, \Phi) = \int_0^1 \mathbb{E}_{P(\mathbf{z}|\mathbf{x}^{(b)},\mathbf{f},\Phi,t)} \left[\log P(\mathbf{x}^{(b)} | \mathbf{z}, \Phi) \right] dt \quad (50)$$

A.4.6 DISCRETIZING THE THERMODYNAMIC INTEGRAL

Here, t_k denotes the tempering at the k -th index of the schedule, and N_t is the number of temperatures. As derived by Calderhead & Girolami (2009), Eq. 28 then be evaluated using:

$$\log \left(P(\mathbf{x}^{(b)} \mid \mathbf{f}, \Phi) \right) = \frac{1}{2} \sum_{k=1}^{N_t} \Delta t_k (E_{k-1} + E_k) + \frac{1}{2} \sum_{k=1}^{N_t} D_{\text{KL}}(P_{t_{k-1}} \parallel P_{t_k}) - D_{\text{KL}}(P_{t_k} \parallel P_{t_{k-1}}) \quad (51)$$

Where:

$$\begin{aligned} \Delta t_k &= t_k - t_{k-1}, & E_k &= \mathbb{E}_{P(\mathbf{z} \mid \mathbf{x}^{(b)}, \mathbf{f}, \Phi, t_k)} \left[\log \left(P(\mathbf{x}^{(b)} \mid \mathbf{z}, \Phi) \right) \right], \\ D_{\text{KL}}(P_{t_{k-1}} \parallel P_{t_k}) &= \mathbb{E}_{P(\mathbf{z} \mid \mathbf{x}^{(b)}, \mathbf{f}, \Phi, t_{k-1})} \left[\log \left(\frac{P(\mathbf{z} \mid \mathbf{x}^{(b)}, \mathbf{f}, \Phi, t_{k-1})}{P(\mathbf{z} \mid \mathbf{x}^{(b)}, \mathbf{f}, \Phi, t_k)} \right) \right] \end{aligned} \quad (52)$$

This reflects the trapezium rule for numerical integration, supported by bias correction to provide an estimate of the Riemann integral that is especially robust to error. The learning gradient derived from the discretized Thermodynamic Integral is unchanged from the MLE gradient in Eq. 16, as demonstrated under Sec. A.4.7.

A.4.7 LEARNING GRADIENT FOR DISCRETIZED THERMODYNAMIC INTEGRAL AND POWER POSTERIOR PARTITION FUNCTION

We can derive the learning gradient of the discretized Thermodynamic Integral in Eq. 51 by reducing it down into a sum of normalizing constants. Starting from the definitions attributed to the KL divergence terms:

$$\begin{aligned} D_{\text{KL}}(P_{t_{k-1}} \parallel P_{t_k}) &= \mathbb{E}_{P(\mathbf{z} \mid \mathbf{x}^{(b)}, \mathbf{f}, \Phi, t_{k-1})} \left[\log P(\mathbf{z} \mid \mathbf{x}^{(b)}, \mathbf{f}, \Phi, t_{k-1}) - \log P(\mathbf{z} \mid \mathbf{x}^{(b)}, \mathbf{f}, \Phi, t_k) \right] \\ \text{and } D_{\text{KL}}(P_{t_k} \parallel P_{t_{k-1}}) &= \mathbb{E}_{P(\mathbf{z} \mid \mathbf{x}^{(b)}, \mathbf{f}, \Phi, t_k)} \left[\log P(\mathbf{z} \mid \mathbf{x}^{(b)}, \mathbf{f}, \Phi, t_k) - \log P(\mathbf{z} \mid \mathbf{x}^{(b)}, \mathbf{f}, \Phi, t_{k-1}) \right] \\ &= -\mathbb{E}_{P(\mathbf{z} \mid \mathbf{x}^{(b)}, \mathbf{f}, \Phi, t_k)} \left[\log P(\mathbf{z} \mid \mathbf{x}^{(b)}, \mathbf{f}, \Phi, t_{k-1}) - \log P(\mathbf{z} \mid \mathbf{x}^{(b)}, \mathbf{f}, \Phi, t_k) \right] \end{aligned} \quad (53)$$

We can leverage Eq. 29 to quantify the log-difference in terms of the change in likelihood contribution plus some normalization constant:

$$\log P(\mathbf{z} \mid \mathbf{x}^{(b)}, \mathbf{f}, \Phi, t_{k-1}) - \log P(\mathbf{z} \mid \mathbf{x}^{(b)}, \mathbf{f}, \Phi, t_k) = -\Delta t_k \cdot \log P(\mathbf{x}^{(b)} \mid \mathbf{z}, \Phi) + \log \left(\frac{\mathbf{Z}_{t_k}}{\mathbf{Z}_{t_{k-1}}} \right) \quad (54)$$

The definitions in Eq. 52 can be used to express the KL divergences in terms of the expected likelihoods:

$$\begin{aligned} \therefore D_{\text{KL}}(P_{t_{k-1}} \parallel P_{t_k}) &= -\Delta t_k \cdot \mathbb{E}_{P(\mathbf{z} \mid \mathbf{x}^{(b)}, \mathbf{f}, \Phi, t_{k-1})} \left[\log P(\mathbf{x}^{(b)} \mid \mathbf{z}, \Phi) \right] + \log \left(\frac{\mathbf{Z}_{t_k}}{\mathbf{Z}_{t_{k-1}}} \right) \\ &= -\Delta t_k \cdot E_{k-1} + \log \left(\frac{\mathbf{Z}_{t_k}}{\mathbf{Z}_{t_{k-1}}} \right) \end{aligned} \quad (55)$$

$$\begin{aligned} \text{and } D_{\text{KL}}(P_{t_k} \parallel P_{t_{k-1}}) &= \Delta t_k \cdot \mathbb{E}_{P(\mathbf{z} \mid \mathbf{x}^{(b)}, \mathbf{f}, \Phi, t_k)} \left[\log P(\mathbf{x}^{(b)} \mid \mathbf{z}, \Phi) \right] - \log \left(\frac{\mathbf{Z}_{t_k}}{\mathbf{Z}_{t_{k-1}}} \right) \\ &= \Delta t_k \cdot E_k - \log \left(\frac{\mathbf{Z}_{t_k}}{\mathbf{Z}_{t_{k-1}}} \right) \end{aligned} \quad (56)$$

Substituting back into Eq. 51, we eliminate the expected likelihood terms:

$$\begin{aligned}
\frac{1}{2} \sum_{k=1}^{N_t} D_{\text{KL}}(P_{t_{k-1}} \| P_{t_k}) - D_{\text{KL}}(P_{t_k} \| P_{t_{k-1}}) &= -\frac{1}{2} \sum_{k=1}^{N_t} \Delta t_k (E_{k-1} + E_k) - 2 \log \left(\frac{\mathbf{Z}_{t_k}}{\mathbf{Z}_{t_{k-1}}} \right) \\
\therefore \log \left(P(\mathbf{x}^{(b)} \mid \mathbf{f}, \Phi) \right) &= \frac{1}{2} \sum_{k=1}^{N_t} \Delta t_k (E_{k-1} + E_k) + \frac{1}{2} \sum_{k=1}^{N_t} D_{\text{KL}}(P_{t_{k-1}} \| P_{t_k}) - D_{\text{KL}}(P_{t_k} \| P_{t_{k-1}}) \\
&= \frac{1}{2} \sum_{k=1}^{N_t} \Delta t_k (E_{k-1} + E_k) - \left[\frac{1}{2} \sum_{k=1}^{N_t} \Delta t_k (E_{k-1} + E_k) - 2 \log \left(\frac{\mathbf{Z}_{t_k}}{\mathbf{Z}_{t_{k-1}}} \right) \right] \\
&= \sum_{k=1}^{N_t} \log \left(\frac{\mathbf{Z}_{t_k}}{\mathbf{Z}_{t_{k-1}}} \right) = \sum_{k=1}^{N_t} \log(\mathbf{Z}_{t_k}) - \log(\mathbf{Z}_{t_{k-1}}) \tag{57}
\end{aligned}$$

Following a similar method to Sec. A.4.4 we can use Eq. 37 to express the learning gradient attributed to each normalization constant in a simpler manner:

$$\begin{aligned}
&\mathbb{E}_{P(\mathbf{z} \mid \mathbf{x}^{(b)}, \mathbf{f}, \Phi, t_k)} \left[\nabla_{\mathbf{f}, \Phi} \log P(\mathbf{z} \mid \mathbf{x}^{(b)}, \mathbf{f}, \Phi, t_k) \right] \\
&= \mathbb{E}_{P(\mathbf{z} \mid \mathbf{x}^{(b)}, \mathbf{f}, \Phi, t_k)} \left[t_k \cdot \nabla_{\Phi} \log P(\mathbf{x}^{(b)} \mid \mathbf{z}, \Phi) + \nabla_{\mathbf{f}} \log P(\mathbf{z} \mid \mathbf{f}) \right] - \nabla_{\mathbf{f}, \Phi} \log(\mathbf{Z}_{t_k}) = 0 \\
\therefore \nabla_{\mathbf{f}, \Phi} \log(\mathbf{Z}_{t_k}) &= \mathbb{E}_{P(\mathbf{z} \mid \mathbf{x}^{(b)}, \mathbf{f}, \Phi, t_k)} \left[t_k \cdot \nabla_{\Phi} \log P(\mathbf{x}^{(b)} \mid \mathbf{z}, \Phi) + \nabla_{\mathbf{f}} \log P(\mathbf{z} \mid \mathbf{f}) \right] \tag{58}
\end{aligned}$$

Telescoping the sum in Eq. 57, and noting that $k = 1$ corresponds to the power posterior equaling the prior, and $k = N_t$ to the posterior, Eq. 57 yields T-KAM's learning gradient:

$$\begin{aligned}
\nabla_{\mathbf{f}, \Phi} \log \left(P(\mathbf{x}^{(b)} \mid \mathbf{f}, \Phi) \right) &= \sum_{k=1}^{N_t} \nabla_{\mathbf{f}, \Phi} \log(\mathbf{Z}_{t_k}) - \nabla_{\mathbf{f}, \Phi} \log(\mathbf{Z}_{t_{k-1}}) \\
&= \nabla_{\mathbf{f}, \Phi} \log(\mathbf{Z}_{t_{N_t}}) - \nabla_{\mathbf{f}, \Phi} \log(\mathbf{Z}_{t_0}) \\
&= \mathbb{E}_{P(\mathbf{z} \mid \mathbf{x}^{(b)}, \mathbf{f}, \Phi)} \left[\nabla_{\mathbf{f}} \log P(\mathbf{z} \mid \mathbf{f}) + \nabla_{\Phi} \log P(\mathbf{x}^{(b)} \mid \mathbf{z}, \Phi) \right] \\
&\quad - \underbrace{\mathbb{E}_{P(\mathbf{z} \mid \mathbf{f})} \left[\nabla_{\mathbf{f}} [\log P(\mathbf{z} \mid \mathbf{f})] \right]}_{=0 \text{ (Eq. 37)}}. \tag{59}
\end{aligned}$$

A.5 HYPERPARAMETERS AND TRAINING DETAILS

Table 4: Hyperparameters for Sec. 3.1.1.

EBM Prior		
layer_widths	p, q	40, 81
spline_type	(-)	variable
spline_activation	(-)	Silu
layer_norm	(-)	false
quadrature_method	(-)	gausslegendre
spline_degree	d	3
grid_size	N_{grid}	RBF: 20 FFT: 50
grid_update_ratio	α_{grid}	0.05
grid_range	$[z_{\min}, z_{\max}]$	Uniform: $[0, 1]$ Lognormal: $[0, 4]$ Gaussian: $[-1.2, 1.2]$
Spline basis ε init.	ε	0.1
Spline basis μ scaling	μ	1.0
Basis activation scaling	σ_b	1.0
Basis spline scaling	σ_s	1.0
Initial basis param.	τ_0	1.0
Train basis param.	$\tau_{\text{trainable}}$	true
GaussQuad_nodes	N_{quad}	100
Use mixture prior	(-)	false
KAN Likelihood		
hidden_widths	$q, 2q + 1$	81, 162
All other KAN hparams	Identical to EBM Prior	
generator_noise	σ_ϵ	0.1
generator_variance	σ_{llhood}	0.1
output_activation	σ_{act}	sigmoid
Importance sampling resampler	resampler	residual
ESS threshold	γ	0.5
Grid updating		
update_prior_grid	(-)	true
update_llhood_grid	(-)	true
num_grid_updating_samples	(-)	100
grid_update_frequency	(-)	100
grid_update_decay	(-)	0.999
Training		
batch_size	N_x	100
importance_sample_size	N_s	100
Training examples	N_{train}	50,000
Testing examples	N_{test}	100
num_generated_samples	(-)	3,000
Number of epochs	N_{epochs}	10
eps	ϵ	0.001
Optimizer		
type	(-)	adam
learning_rate	η_{LR}	0.001
betas	(-)	(0.9, 0.999)

Table 5: Hyperparameters for Sec. 3.1.2.

EBM Prior		
layer_widths	p, q	40, 81
spline_type	(-)	variable
spline_activation	(-)	Silu
layer_norm	(-)	false
quadrature_method	(-)	gausslegendre
spline_degree	d	3
grid_size	N_{grid}	RBF: 20 FFT: 50
grid_update_ratio	α_{grid}	0.05
grid_range	$[z_{\min}, z_{\max}]$	Uniform: $[0, 1]$ Lognormal: $[0, 4]$ Gaussian: $[-1.2, 1.2]$
Spline basis ε init.	ε	0.1
Spline basis μ scaling	μ	1.0
Basis activation scaling	σ_b	1.0
Basis spline scaling	σ_s	1.0
Initial basis param.	τ_0	1.0
Train basis param.	$\tau_{\text{trainable}}$	true
GaussQuad_nodes	N_{quad}	100
Use mixture prior	(-)	false
KAN Likelihood		
hidden_widths	$q, 2q + 1$	81, 162
All other KAN hparams	Identical to EBM Prior	
generator_noise	σ_ε	0.1
generator_variance	σ_{llhood}	0.1
output_activation	σ_{act}	sigmoid
Importance sampling resampler	resampler	residual
ESS threshold	γ	0.5
Grid updating		
update_prior_grid	(-)	true
update_llhood_grid	(-)	true
num_grid_updating_samples	(-)	100
grid_update_frequency	(-)	100
grid_update_decay	(-)	0.999
Training		
batch_size	N_x	100
importance_sample_size	N_s	100
Training examples	N_{train}	1,000
Testing examples	N_{test}	1,000
num_generated_samples	(-)	3,000
Number of epochs	N_{epochs}	1,000
eps	ϵ	0.001
Optimizer		
type	(-)	adam
learning_rate	η_{LR}	0.001
betas	(-)	(0.9, 0.999)

Table 6: Hyperparameters for Sec. 3.2.

EBM Prior		
layer_widths	p, q	See Sec. A.5.1
spline_type	(-)	Cheby
spline_activation	(-)	None
layer_norm	(-)	false
quadrature_method	(-)	gausslegendre
spline_degree	d	5
grid_size	N_{grid}	1
grid_update_ratio	α_{grid}	N/A
grid_range	$[z_{\text{min}}, z_{\text{max}}]$	$[-1, 1]$
Spline basis ε init.	ε	0.1
Spline basis μ scaling	μ	1.0
Basis activation scaling	σ_b	1.0
Basis spline scaling	σ_s	1.0
Initial basis param.	τ_0	1.001
Train basis param.	$\tau_{\text{trainable}}$	false
GaussQuad_nodes	N_{quad}	200
Use mixture prior	(-)	true
KAN Likelihood		
cnn_widths	(-)	See Sec. A.5.1
All other KAN hparams	N/A, an MLP CNN was used	
generator_noise	σ_ϵ	0.01
generator_variance	σ_ϵ	0.25
output_activation	σ_{act}	sigmoid
Importance sampling resampler	resampler	Not used
ESS threshold	γ	N/A
VGG16 perceptual loss scale, perceptual_scale	(-)	N/A
Grid updating		
update_prior_grid	(-)	true
update_llhood_grid	(-)	false
Training		
batch_size	N_x	100
importance_sample_size	N_s	N/A
Training examples	N_{train}	20,000
Testing examples	N_{test}	100
num_generated_samples	(-)	3,000
Number of epochs	N_{epochs}	40
eps	ϵ	0.0001
Use VGG16 perceptual loss, use_perceptual_loss	(-)	false
Optimizer		
type	(-)	adam
learning_rate	η_{LR}	0.0002
betas	(-)	(0.9, 0.999)
POSTERIOR LANGEVIN		
iters	N_{local}	40
step_size	η	0.002
THERMODYNAMIC INTEGRATION		
iters	N_{local}	(see posterior langevin)
num_temps	N_t	10
Initial exponent in power law schedule	p_{start}	10
Final exponent in power law schedule	p_{end}	3
Number of cosine cycles	N_{cycles}	0
Global swap frequency, replica_exchange_frequency	(-)	1

A.5.1 SVHN & CELEBA ARCHITECTURES

Table 7: The dense Chebyshev KAN network used as the mixture prior model

Layer	Operation	Output Dim.
Input	Sample z	$p = 20$
Energy functions	Dense(20)	$q = 41$

sizes=[20, 41]

Table 8: CNN Generator Architecture for SVHN (32×32)

Layer	Operation	Output Shape	Stride
Input	Latent vector z reshaped	$1 \times 1 \times q$	–
1	4×4 convT(256), LeakyReLU	$4 \times 4 \times 256$	1
2	4×4 convT(128), LeakyReLU	$8 \times 8 \times 128$	2
3	4×4 convT(64), LeakyReLU	$16 \times 16 \times 64$	2
4	4×4 convT(3), Sigmoid	$32 \times 32 \times 3$	2

Config: kernel=4, 4, 4, 4 strides=1/2/2/2, paddings=0/1/1/1, activation=LeakyReLU, batchnorm=False

Table 9: CNN Generator Architecture for CelebA (64×64)

Layer	Operation	Output Shape	Stride
Input	Latent vector z reshaped	$1 \times 1 \times q$	–
1	4×4 convT(512), LeakyReLU	$4 \times 4 \times 512$	1
2	4×4 convT(256), LeakyReLU	$8 \times 8 \times 256$	2
3	4×4 convT(128), LeakyReLU	$16 \times 16 \times 128$	2
4	4×4 convT(64), LeakyReLU	$32 \times 32 \times 64$	2
5	4×4 convT(3), Sigmoid	$64 \times 64 \times 3$	2

Config: kernel=4, 4, 4, 4, 4 strides=1/2/2/2/2, paddings=0/1/1/1/1, activation=LeakyReLU, batchnorm=False

A.6 SAMPLING THEORY

This section provides more theoretical detail regarding T-KAM’s sampling procedures.

A.6.1 IMPORTANCE SAMPLING

Importance Sampling (IS) is a Monte Carlo method rooted in the measure-theoretic formulation of probability. It enables the estimation of expectations with respect to one probability measure using samples drawn from another. For a detailed exposition, see Kloek & van Dijk (1978).

The Radon-Nikodym derivative

IS involves rewriting the expectation of an arbitrary function, $\rho(z)$, under the target measure, $P(z)$, in terms of a more tractable proposal measure, $Q(z)$. Specifically, we use the Radon-Nikodym derivative $\frac{dP}{dQ}$ to rewrite the expectation of an arbitrary function of z , denoted as $\rho(z)$:

$$\mathbb{E}_{P(z)}[\rho(z)] = \int_{\bar{z}} \rho(z) dP(z) = \int_{\bar{z}} \rho(z) \cdot \frac{dP}{dQ} dQ(z). \quad (60)$$

Here, $\frac{dP}{dQ}$ acts as a weight that adjusts the contribution of each sample to account for the difference between the target and proposal measures. This requires that the proposal measure Q is absolutely

continuous with respect to the target measure P , i.e. $Q(A) = 0$ implies $P(A) = 0$, for every measurable subset $A \in \mathcal{Z}$.

In the context of T-KAM, the target distribution is the posterior, $P(\mathbf{z} \mid \mathbf{x}^{(b)}, \mathbf{f}, \Phi)$, which is proportional to the product of the likelihood and the prior:

$$P(\mathbf{z} \mid \mathbf{x}^{(b)}, \mathbf{f}, \Phi) \propto P(\mathbf{x}^{(b)} \mid \mathbf{z}, \Phi) \cdot P(\mathbf{z} \mid \mathbf{f}). \quad (61)$$

The exact normalization constant, (the marginal likelihood $P(\mathbf{x}^{(b)} \mid \mathbf{f}, \Phi)$), is intractable, but Importance Sampling circumvents the need to compute it explicitly. Instead, the expectation of $\rho(\mathbf{z})$ under the posterior can be expressed as:

$$\mathbb{E}_{P(\mathbf{z} \mid \mathbf{x}^{(b)}, \mathbf{f}, \Phi)}[\rho(\mathbf{z})] = \int_{\bar{\mathcal{Z}}} \rho(\mathbf{z}) w(\mathbf{z}) dQ(\mathbf{z}), \quad (62)$$

where the importance weights $w(\mathbf{z})$ are given by:

$$w(\mathbf{z}) = \frac{P(\mathbf{z} \mid \mathbf{x}^{(b)}, \mathbf{f}, \Phi)}{Q(\mathbf{z})} = \frac{P(\mathbf{x}^{(b)} \mid \mathbf{z}, \Phi) \cdot P(\mathbf{z} \mid \mathbf{f})}{Q(\mathbf{z})}. \quad (63)$$

Proposal distribution and importance weights

A practical choice for the proposal distribution $Q(\mathbf{z})$ is the prior, $P(\mathbf{z} \mid \mathbf{f})$, given the availability of draws from the prior using the method outlined in Sec. 2.4.3. This simplifies the importance weights, as the prior has a tractable form and covers the support of the posterior. This yields:

$$w(\mathbf{z}^{(s)}) = P(\mathbf{x}^{(b)} \mid \mathbf{z}^{(s)}, \Phi) \propto \exp(\log(P(\mathbf{x}^{(b)} \mid \mathbf{z}^{(s)}, \Phi))). \quad (64)$$

This reflects that the likelihood now directly informs how much weight to assign to each sample \mathbf{z} . Intuitively, samples that better explain the observed data $\mathbf{x}^{(b)}$, (as measured by the likelihood), are given higher importance. Using the definition of softmax, the normalized weights are given by:

$$\frac{w(\mathbf{z}^{(s)})}{\sum_{r=1}^{N_s} w(\mathbf{z}^{(r)})} = \text{softmax}_s \left(\log(P(\mathbf{x}^{(b)} \mid \mathbf{z}^{(s)}, \Phi)) \right). \quad (65)$$

Resampling

The suitability of these weights depends on how well $Q(\mathbf{z})$ matches the posterior. In T-KAM, there is likely to be significant mismatch due to the complexity of the likelihood models described in Eq. 20. Consequently, the weights will exhibit high variance, resulting in many samples contributing minimally. This reduces the Effective Sample Size (ESS) and introduces bias into the estimates.

To address this, the weights are resampled before proceeding with the posterior expectation. This is accomplished by using one of the methods outlined by Douc et al. (2005), whenever the ESS falls below a certain threshold determined by Eq. 26. Resampling redistributes the sample weights, creating a new population with uniformly distributed weights while preserving the statistical properties of the original distribution. As training progresses and the prior becomes a better match for the posterior, the need for resampling decreases.

Importance Sampling estimator

To estimate the expectation, we draw N_s independent samples $\{\mathbf{z}^{(s)}\}_{s=1}^{N_s} \sim Q(\mathbf{z})$ using the procedure outlined in Sec. 2.4.3 and compute a weighted sum:

$$\mathbb{E}_{P(\mathbf{z} \mid \mathbf{x}^{(b)}, \mathbf{f}, \Phi)}[\rho(\mathbf{z})] \approx \sum_{s=1}^{N_s} \rho(\mathbf{z}_{\text{resampled}}^{(s)}) \cdot w_{\text{norm, resampled}}(\bar{\mathbf{z}}_{\text{resampled}}^{(s)}). \quad (66)$$

The estimator is unbiased, implying that its expectation matches the true posterior expectation. As $N_s \rightarrow \infty$, the approximation converges almost surely to the true value, provided that $Q(\mathbf{z})$ sufficiently covers the posterior to ensure a well-conditioned Radon-Nikodym derivative. This estimator is used for the log-marginal likelihood and its gradient in Eqs. 15 & 16, since it provides a means of estimating expectations with respect to the posterior distribution.

A.6.2 RESIDUAL RESAMPLING

In this study, we adopted residual resampling to redraw weights. This redistributes the population of latent samples according to the normalized weights of Sec. A.6.1. The procedure is only conducted when Eq. 26 regarding ESS is satisfied:

1. **Integer replication:** The sample, s , is replicated r_s times, where:

$$r_s = \left\lfloor N_s \cdot w_{\text{norm}}(\mathbf{z}^{(s)}) \right\rfloor \quad (67)$$

2. **Residual weights:** The total number of replicated samples after the previous stage will be $\sum_{s=1}^{N_s} r_s$. Therefore, $N_s - \sum_{s=1}^{N_s} r_s$ remain, which must be resampled using the residuals:

$$w_{\text{residual}}(\mathbf{z}^{(s)}) = w_{\text{norm}}(\mathbf{z}^{(s)}) \cdot (N_s - r_s)$$

$$w_{\text{norm, residual}}(\mathbf{z}^{(s)}) = \frac{w_{\text{residual}}(\mathbf{z}^{(s)})}{\sum_{s=1}^{N_s} w_{\text{residual}}(\mathbf{z}^{(s)})} \quad (68)$$

If a sample has been replicated at the previous stage, then its corresponding $w_{\text{norm, residual}}$ will be reduced, leading to a lower probability of it being resampled again.

3. **Resample:** The remaining samples are drawn with multinomial resampling, based on the cumulative distribution function of the residuals:

$$k^* = \min \left\{ j \mid \sum_{s=1}^j w_{\text{norm, residual}}(\mathbf{z}^{(s)}) \geq u_i \right\} \quad \text{where } u_i \sim \mathcal{U}([0, 1]). \quad (69)$$

where k^* represents the index of the sample to keep.

A.6.3 METROPOLIS-ADJUSTED LANGEVIN ALGORITHM (MALA)

The Metropolis-Adjusted Langevin Algorithm (MALA) (Rosky et al., 1978a; Zhu & Mumford, 1998), is a Markov Chain Monte Carlo (MCMC) method designed to sample from complex distributions by leveraging gradient information. It constructs a proposal mechanism that efficiently explores the target measure by combining stochastic perturbations with information from the target's local geometry to propose local moves, thereby refining the standard Metropolis-Hastings (MH) algorithm (Hastings, 1970).

MALA operates on the target (power) posterior $P(\mathbf{z} \mid \mathbf{x}^{(b)}, \mathbf{f}, \Phi, t_k)$. The algorithm constructs a sequence of random variables $\{\mathbf{z}^{(i, t_k)}\}_{i=1}^{\infty}$ that forms a Markov chain converging in distribution to the target measure. The target posterior measure, $P(\mathbf{z} \mid \mathbf{x}^{(b)}, \mathbf{f}, \Phi, t_k)$, is:

$$\log P(\mathbf{z} \mid \mathbf{x}^{(b)}, \mathbf{f}, \Phi, t_k) = \log P(\mathbf{x}^{(b)} \mid \mathbf{z}, \Phi)^{t_k} + \log P(\mathbf{z} \mid \mathbf{f}) - \text{const}, \quad (70)$$

MALA

Starting with the initial state of the first chain, $\mathbf{z}^{(1, t_1)} \sim Q(\mathbf{z}) = P(\mathbf{z} \mid \mathbf{f})$, the local state within a temperature is updated as follows:

1. **Langevin diffusion:** A new state $\mathbf{z}'^{(i, t_k)}$ is proposed for a local chain, operating with a specific t_k , using a transition kernel inspired by (overdamped) Langevin dynamics (Roberts & Stramer, 2002; Brooks et al., 2011):

$$\textbf{Target: } \log \gamma(\mathbf{z}'^{(i, t_k)}) \propto \log P(\mathbf{x}^{(b)} \mid \mathbf{z}, \Phi)^{t_k} + \log P(\mathbf{z} \mid \mathbf{f})$$

$$\textbf{Proposal: } \mathbf{z}'^{(i, t_k)} \mid \mathbf{z}^{(i, t_k)} \sim q(\mathbf{z}'^{(i, t_k)} \mid \mathbf{z}^{(i, t_k)})$$

$$\textbf{Kernel: } q(\mathbf{z}'^{(i, t_k)} \mid \mathbf{z}^{(i, t_k)}) = \mathcal{N}\left(\mathbf{z}'^{(i, t_k)}; \mathbf{z}^{(i, t_k)} + \frac{\eta}{2} \mathbf{C} \cdot \nabla_{\mathbf{z}} \log \gamma(\mathbf{z}'^{(i, t_k)}), \left(\sqrt{\eta} \cdot \mathbf{C}^{\frac{1}{2}}\right)^2\right), \quad (71)$$

where $\eta > 0$ is the step size, $\nabla_{\mathbf{z}} \log \gamma$ is the log-posterior gradient with respect to $\mathbf{z}^{(i, t_k)}$, and \mathbf{C} is a pre-conditioning, positive-definite matrix, (for example, the identity matrix, \mathbf{I}).

2. **MH criterion:** Once $N_{\text{unadjusted}}$ iterations have elapsed, Metropolis-Hastings adjustments, (MH) (Metropolis & Ulam, 1949), are introduced. The criterion for the local proposal is:

$$r_{\text{local}} = \frac{\gamma(\mathbf{z}'^{(i, t_k)}) q(\mathbf{z}^{(i, t_k)} | \mathbf{z}'^{(i, t_k)})}{\gamma(\mathbf{z}^{(i, t_k)}) q(\mathbf{z}'^{(i, t_k)} | \mathbf{z}^{(i, t_k)})}, \quad (72)$$

3. **Acceptance:** The proposal is accepted with probability $\min(1, r_{\text{local}})$. If accepted, $\mathbf{z}^{(i+1, t_k)} = \mathbf{z}'^{(i, t_k)}$; otherwise, the current state is retained: $\mathbf{z}^{(i+1, t_k)} = \mathbf{z}^{(i, t_k)}$.
4. **Global Swaps:** Global swaps are proposed and accepted subject to the criterion outlined in Eq. 34

Convergence

Under mild regularity conditions, the local Markov chain $\{\mathbf{z}^{(i, t_k)}\}$ generated by MALA converges in distribution to $P(\mathbf{z} | \mathbf{x}^{(b)}, \mathbf{f}, \Phi, t_k)$ as $N_{\text{local}} \rightarrow \infty$. The proposal mechanism in Eq. 71 ensures that the chain mixes efficiently, particularly in high-dimensional spaces, provided that the step size η is tuned appropriately. The algorithm provides theoretical guarantees of the target, due to its satisfaction of detailed balance under Eq. 72:

$$\gamma(\mathbf{z}^{(i, t_k)}) q(\mathbf{z}'^{(i, t_k)} | \mathbf{z}^{(i, t_k)}) = \gamma(\mathbf{z}'^{(i, t_k)}) q(\mathbf{z}^{(i, t_k)} | \mathbf{z}'^{(i, t_k)}), \quad (73)$$

ensuring that the stationary distribution of the local chain matches the local target.

A.6.4 AUTOMALA

More details on the Metropolis-adjusted Langevin Algorithm (MALA) are provided in Sec. A.6.3.

Selecting an appropriate step size for unaltered MALA presents a challenge, particularly for SE, as each power posterior exhibits distinct local curvature. To address this, we adaptively tune the step size with autoMALA (Biron-Lattes et al., 2024), which reinterprets MALA as Hamiltonian Monte Carlo (HMC) with a single leapfrog step (Duane et al., 1987).

The algorithm operates locally on a target power posterior $P(\mathbf{z} | \mathbf{x}^{(b)}, \mathbf{f}, \Phi, t_k)$. It constructs a sequence of random variables per temperature, $\{\mathbf{z}^{(i, t_k)}\}_{i=1}^{\infty}$, that forms a Markov chain converging in distribution to the local target:

$$\log \gamma(\mathbf{z}'^{(i, t_k)}) = \log P(\mathbf{z}^{(i, t_k)} | \mathbf{x}^{(b)}, \mathbf{f}, \Phi, t_k) \propto \log P(\mathbf{x}^{(b)} | \mathbf{z}^{(i, t_k)}, \Phi)^{t_k} + \log P(\mathbf{z}^{(i, t_k)} | \mathbf{f}).$$

Starting with the initial state of the first chain, $\mathbf{z}^{(1, t_1)} \sim Q(\mathbf{z}) = P(\mathbf{z} | \mathbf{f})$, the local state within a temperature is updated as follows:

1. **Acceptance thresholds:** Two bounding acceptance thresholds are sampled uniformly:

$$a, b \sim \mathcal{U}\left((a, b); \mathbf{0}, \mathbf{1}\right), \quad (a, b) \in [0, 1]^2, \quad b > a \quad (74)$$

2. **Mass matrix:** Random pre-conditioning matrices are initialized per latent dimension:

$$\varepsilon^{(i, t_k)} \sim \text{Beta}_{01} \left(1, 1; \left[\frac{1}{2}, \frac{2}{3}\right]\right),$$

$$M_{p,p}^{1/2 (i, t_k, q)} = \varepsilon^{(i, t_k)} \cdot \Sigma_{p,p}^{-1/2 (i, t_k, q)} + (1 - \varepsilon^{(i, t_k)}), \quad (75)$$

where $\Sigma_{p,p}^{(i, t_k, q)} = \text{VAR}_s \left[\bar{z}_{q,p}^{(i, t_k, s)} \right]$. Here, $\text{Beta}_{01} [a, b; c, d]$ denotes a zero-one-inflated Beta distribution. The parameters $a, b > 0$ represent the shape parameters of the Beta distribution, while $c, d \in [0, 1]^2$ specify the probabilities governing the mixture. The positive definite mass matrix, M , can be related to Eq. 71 as $M = C^{-1}$, and is efficient to invert as a diagonal matrix.

3. **Leapfrog proposal:** The following transition is proposed for a local chain, t_k , with an adaptive step size, $\eta^{(i, t_k)}$:

$$\begin{aligned}
\mathbf{p}^{(i, t_k)} &\sim \mathcal{N}(\mathbf{p}; \mathbf{0}, \mathbf{M}^{(i, t_k)}) \\
\mathbf{p}'_{1/2} &= \mathbf{p}^{(i, t_k)} + \frac{\eta^{(i, t_k)}}{2} \nabla_{\mathbf{z}} \log \gamma(\mathbf{z}'^{(i, t_k)}) \\
\mathbf{z}'^{(i, t_k)} &= \mathbf{z}^{(i, t_k)} + \eta^{(i, t_k)} \left(\mathbf{M}^{-1} \mathbf{p}'_{1/2} \right)^{(i, t_k)} \\
\hat{\mathbf{p}}^{(i, t_k)} &= \mathbf{p}'_{1/2} + \frac{\eta^{(i, t_k)}}{2} \nabla_{\mathbf{z}} \log \gamma(\mathbf{z}'^{(i, t_k)}) \\
\mathbf{p}'^{(i, t_k)} &= -\hat{\mathbf{p}}^{(i, t_k)},
\end{aligned} \tag{76}$$

4. **MH criterion:** Once $N_{\text{unadjusted}}$ iterations have elapsed, Metropolis-Hastings (MH) adjustments are introduced. The MH acceptance criterion for the local proposal is:

$$r_{\text{local}} = \frac{\gamma(\mathbf{z}'^{(i, t_k)}) \mathcal{N}(\mathbf{p}'^{(i, t_k)}; \mathbf{0}, \mathbf{M}^{(i, t_k)})}{\gamma(\mathbf{z}^{(i, t_k)}) \mathcal{N}(\mathbf{p}^{(i, t_k)}; \mathbf{0}, \mathbf{M}^{(i, t_k)})}, \tag{77}$$

5. **Step size adaptation:** Starting with an initial estimate, $\eta_{\text{init}}^{(i, t_k)}$, set as the average accepted step size from the previous training iteration, (used as a simple alternative to the round-based tuning algorithm proposed by Biron-Lattes et al. (2024)), the step size is adjusted as follows:

- If $a < r_{\text{local}} < b$, then $\eta^{(i, t_k)} = \eta_{\text{init}}^{(i, t_k)}$
- If $r_{\text{local}} \leq a$, then $\eta'^{(i, t_k)} = \eta_{\text{init}}^{(i, t_k)} / \Delta \eta^k$, where $k \leftarrow k + 1$ is chosen recursively until $r_{\text{local}} > a$, and the step size is accepted, $\eta^{(i, t_k)} = \eta'^{(i, t_k)}$
- If $r_{\text{local}} \geq b$, then $\eta'^{(i, t_k)} = \eta_{\text{init}}^{(i, t_k)} \cdot \Delta \eta^k$, where $k \leftarrow k + 1$ is chosen recursively until $r_{\text{local}} < b$, and the step size is accepted, $\eta^{(i, t_k)} = \eta'^{(i, t_k)} / \Delta \eta$

Here, $\Delta \eta$ is a tunable hyperparameter that controls the rate of step size adaptation. To improve efficiency in our implementation, tuning is prematurely terminated when $\eta^{(i, t_k)}$ falls out of a user-defined range, $[\eta_{\text{min}}, \eta_{\text{max}}]$. Excessively large or small step sizes are not beneficial, so preventing the algorithm from searching extreme values saves time without compromising performance.

6. **Reversibility check:** If the step size was modified, the reversibility of the update in Eq. 76 is verified before proceeding with MH acceptance. If $\eta_{\text{init}}^{(i, t_k)}$ cannot be recovered from the reversed step-size adjustment process with the proposed state, $\{\mathbf{z}'^{(i, t_k)}, \mathbf{p}'^{(i, t_k)}, \eta^{(i, t_k)}\}$, the proposal is rejected regardless of the outcome of the MH adjustment.

7. **Acceptance:** The proposal is accepted with probability $\min(1, r_{\text{local}})$. If accepted, $\mathbf{z}^{(i+1, t_k)} = \mathbf{z}'^{(i, t_k)}$; otherwise, the current state is retained: $\mathbf{z}^{(i+1, t_k)} = \mathbf{z}^{(i, t_k)}$.

8. **Global Swaps:** Global swaps are proposed and accepted subject to Eq. 34

A.7 EXTRA IMAGE SAMPLES

A.7.1 MNIST

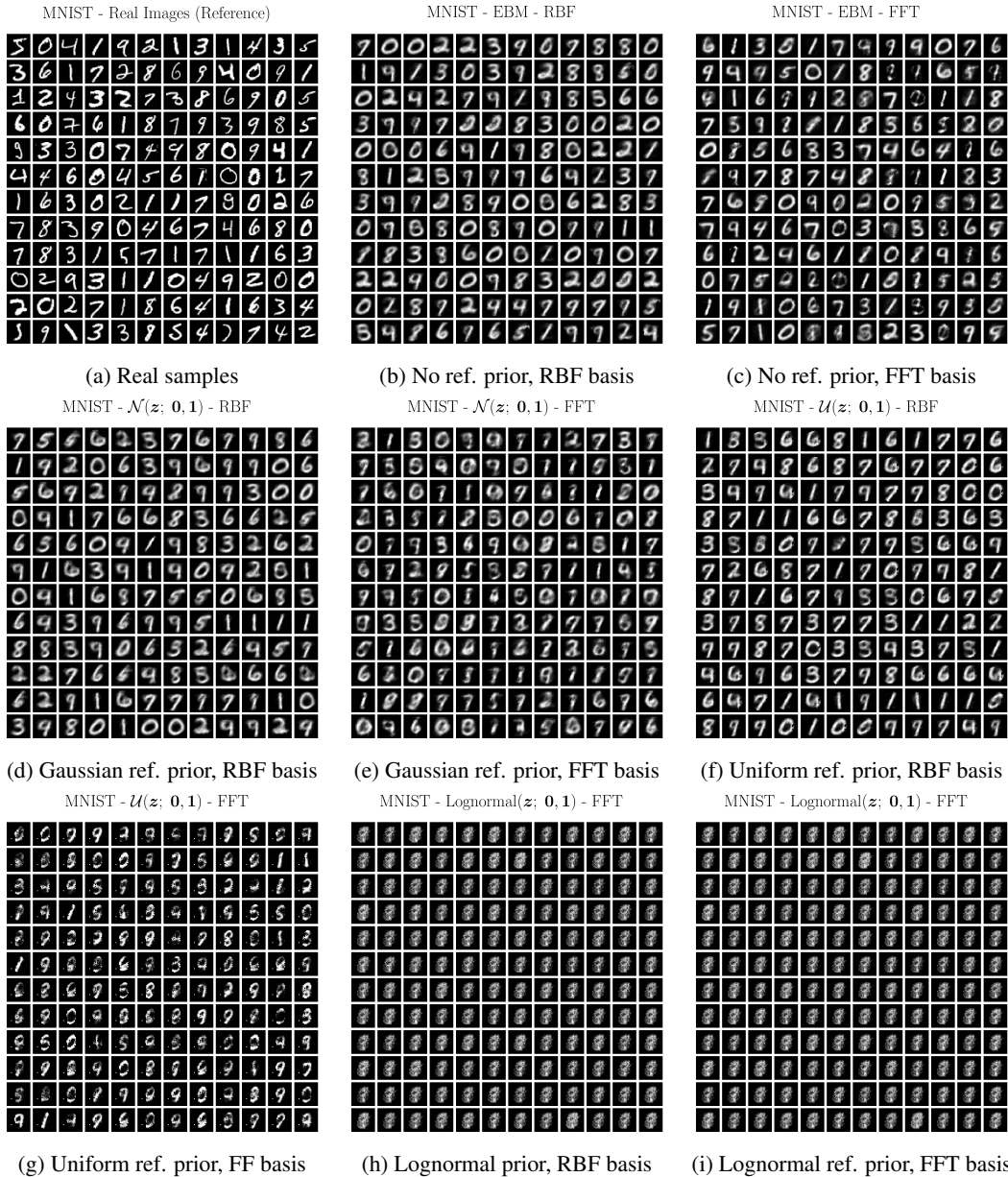


Figure 12: Generated MNIST examples using different bases and exponentially-tilted priors (Sec. 3.1.1).

A.7.2 FMNIST

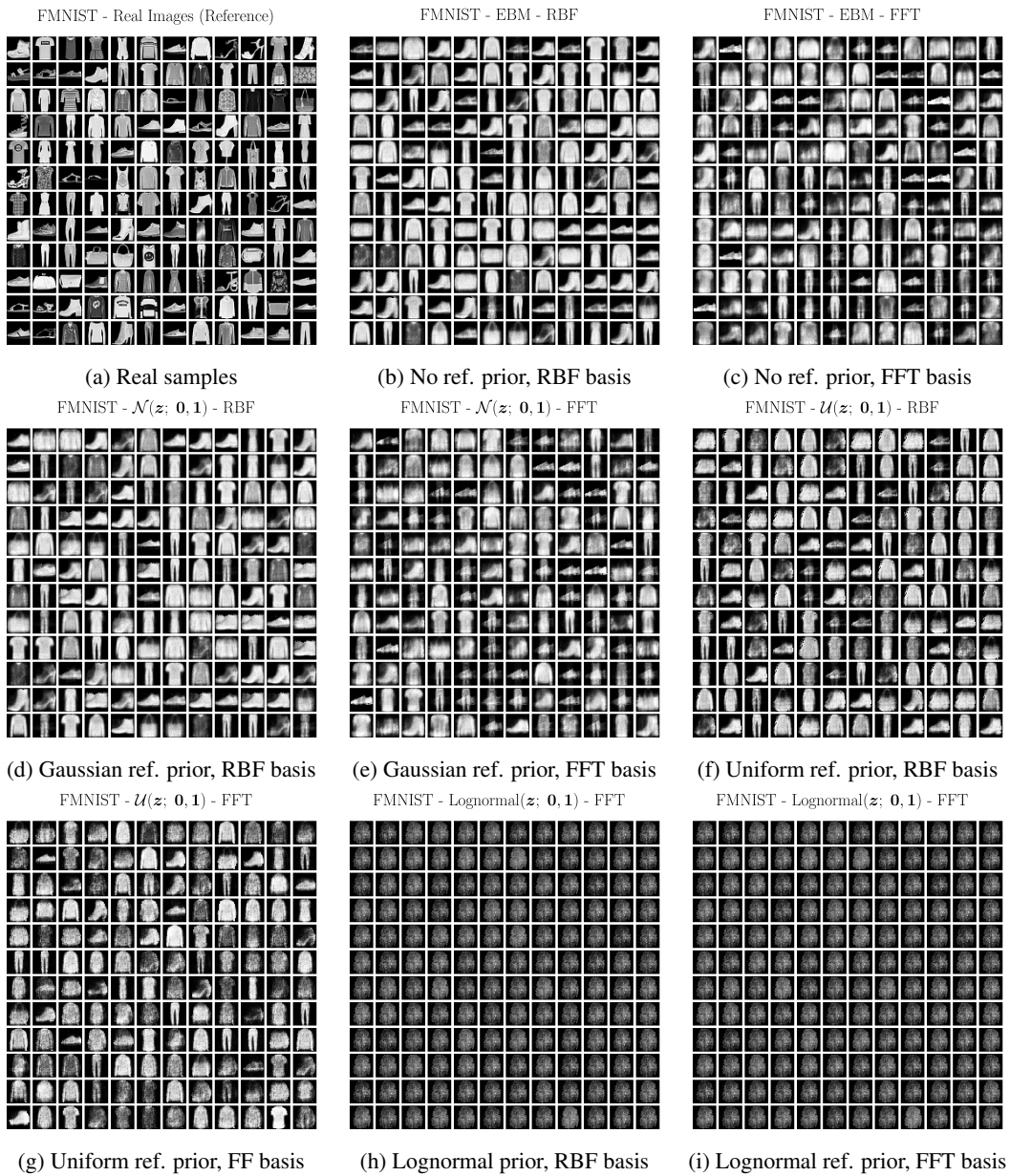


Figure 13: Generated FMNIST examples using different bases and exponentially-tilted priors (Sec. 3.1.1).

A.7.3 DARCY FLOW

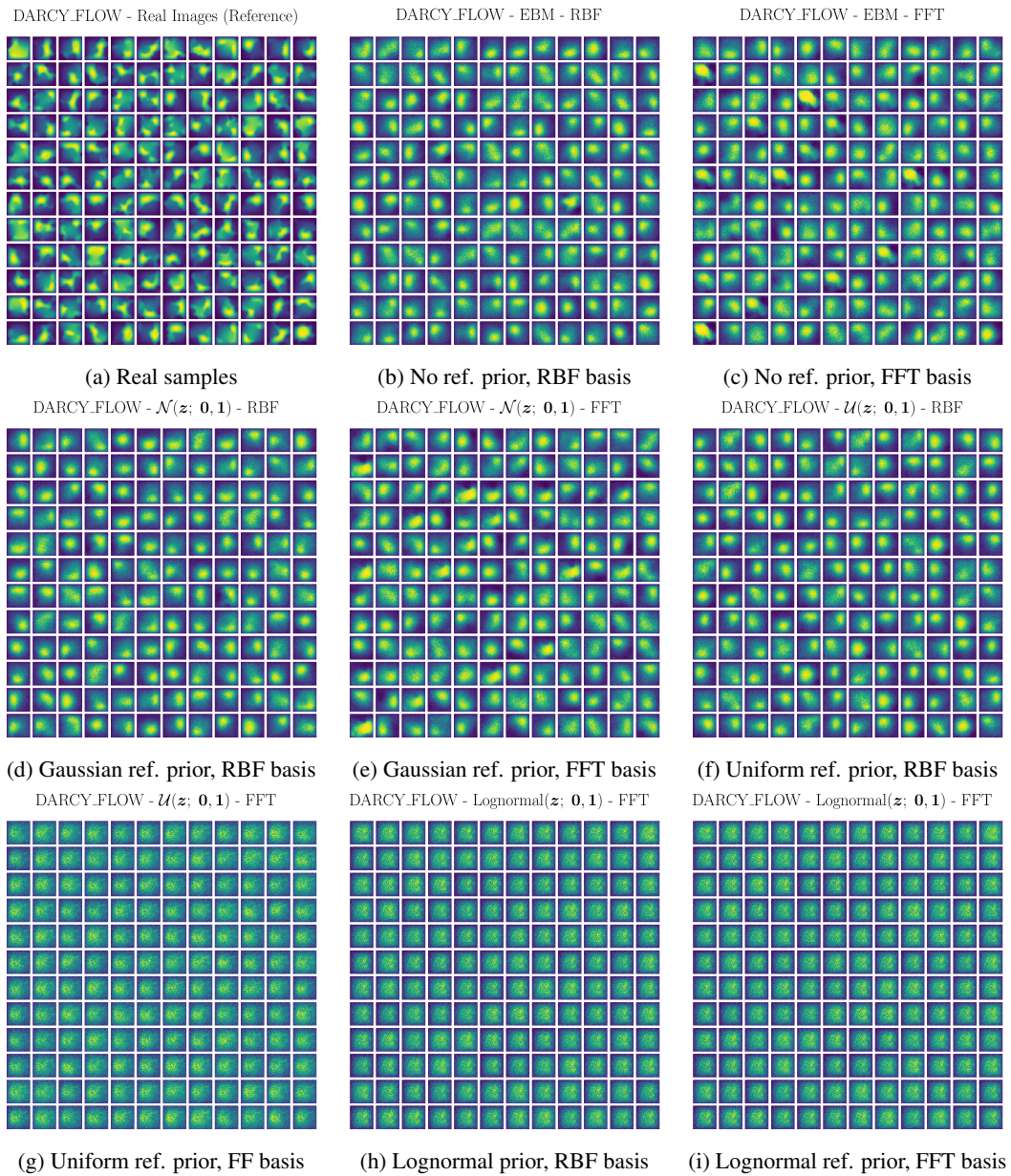


Figure 14: Generated Darcy flow examples using different bases and exponentially-tilted priors (Sec. 3.1.2).

A.7.4 SVHN

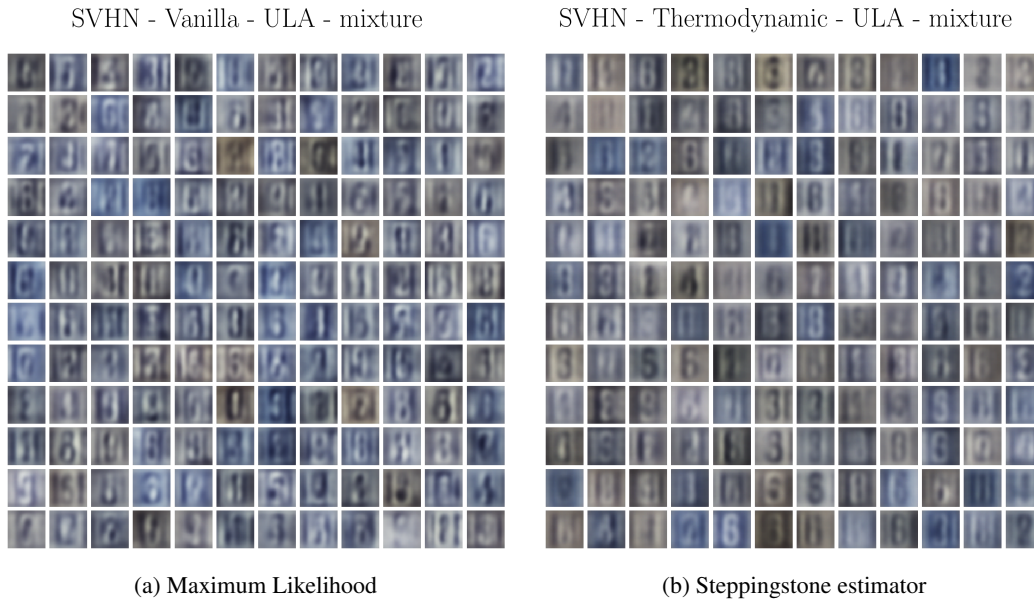


Figure 15: Generated SVHN examples by T-KAM trained with MLE and SE.

A.7.5 CELEBA

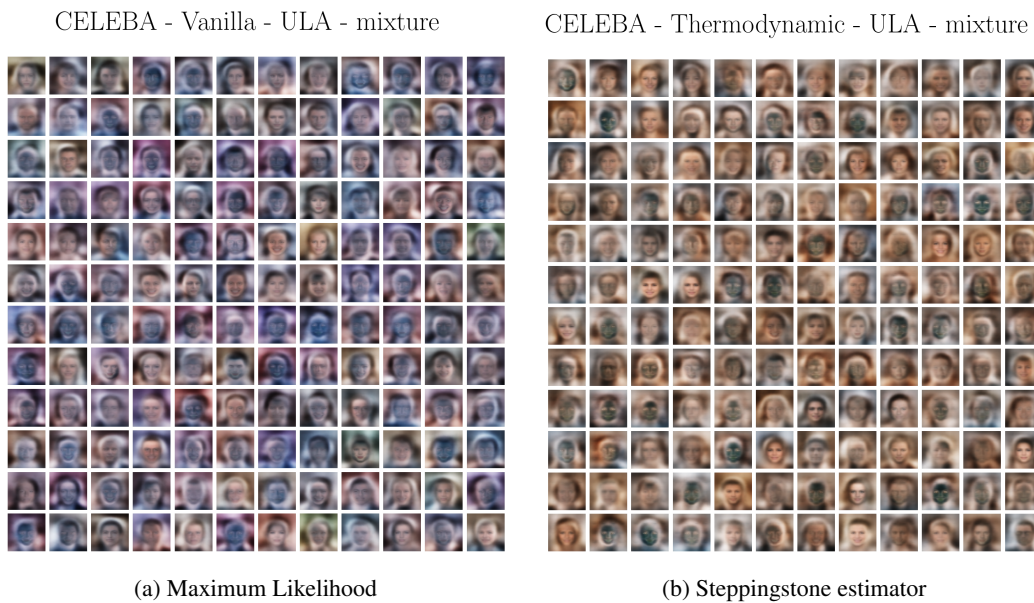


Figure 16: Generated CelebA examples by T-KAM trained with MLE and SE.

A.8 TRAINED LATENT PRIORS

The following priors were extracted from trained T-KAM models, each corresponding to the first three components of prior $q = 1$.

A.8.1 MNIST RBF

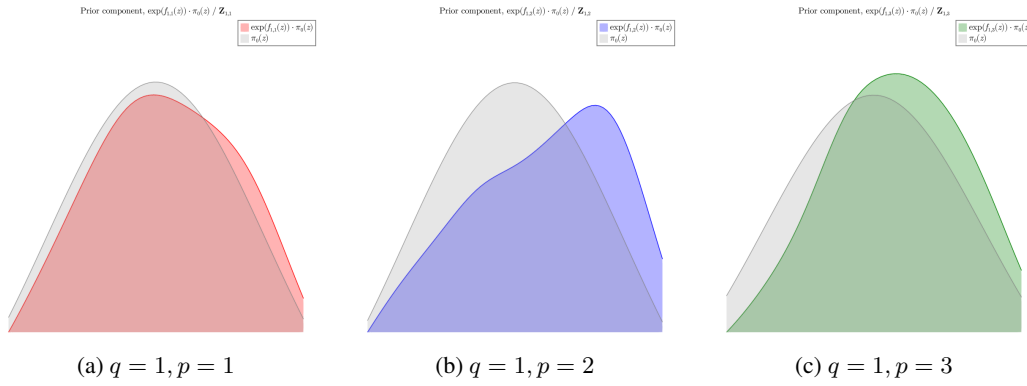


Figure 17: Three components from T-KAM's prior after training on MNIST for 5,000 parameter updates with RBF bases and Gaussian constrained priors.

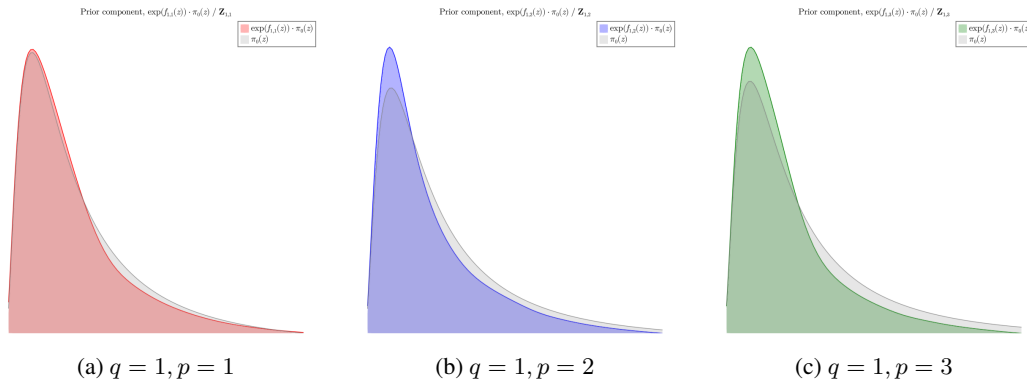


Figure 18: Three components from T-KAM's prior after training on MNIST for 5,000 parameter updates with RBF bases and lognormal constrained priors.

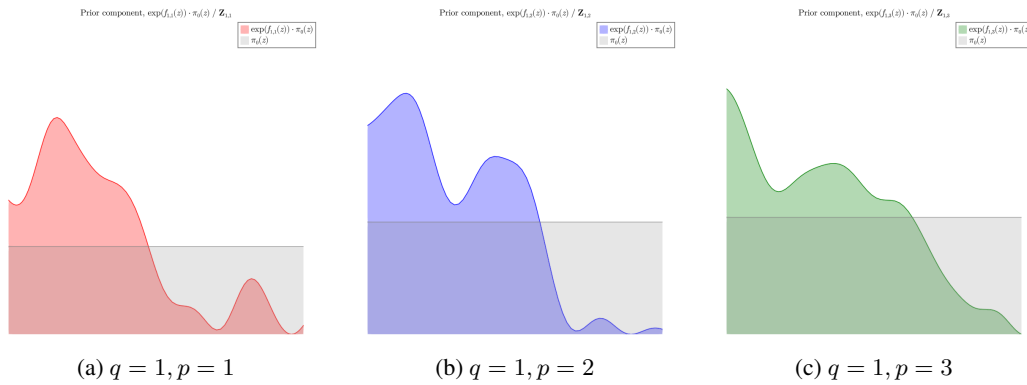


Figure 19: Three components from T-KAM's prior after training on MNIST for 5,000 parameter updates with RBF bases and uniform constrained priors.

A.8.2 MNIST FFT

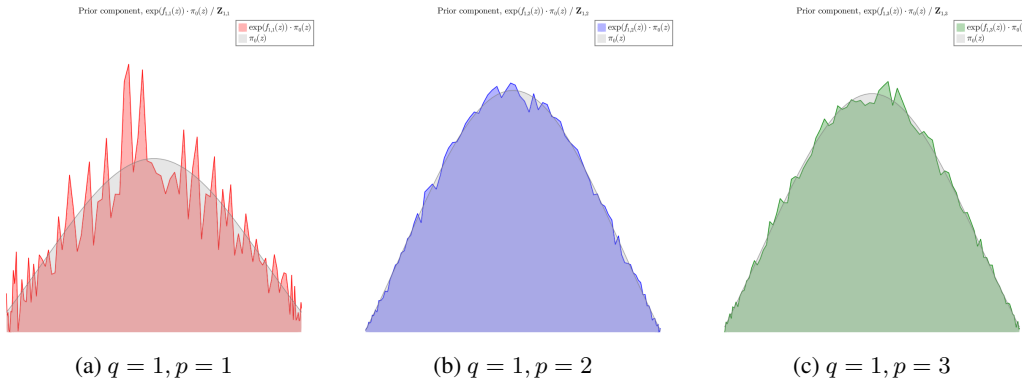


Figure 20: Three components from T-KAM's prior after training on MNIST for 5,000 parameter updates with FFT bases and Gaussian constrained priors.

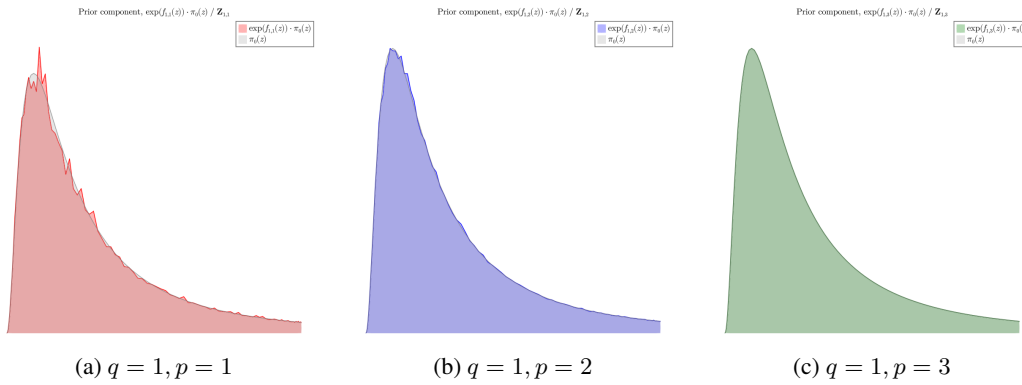


Figure 21: Three components from T-KAM's prior after training on MNIST for 5,000 parameter updates with FFT bases and lognormal constrained priors.

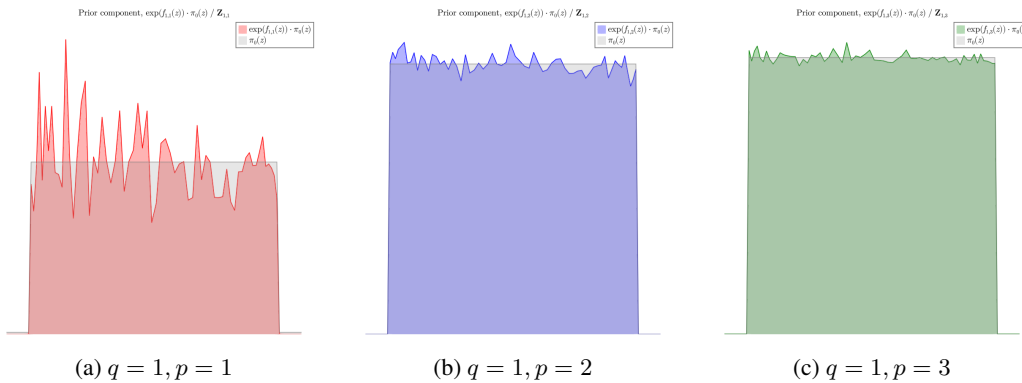


Figure 22: Three components from T-KAM's prior after training on MNIST for 5,000 parameter updates with FFT bases and uniform constrained priors.

A.8.3 FMNIST RBF

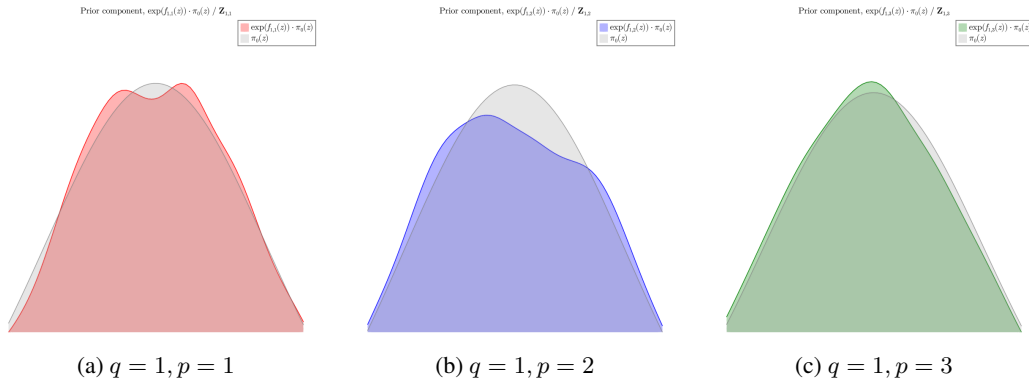


Figure 23: Three components from T-KAM's prior after training on FMNIST for 5,000 parameter updates with RBF bases and Gaussian constrained priors.

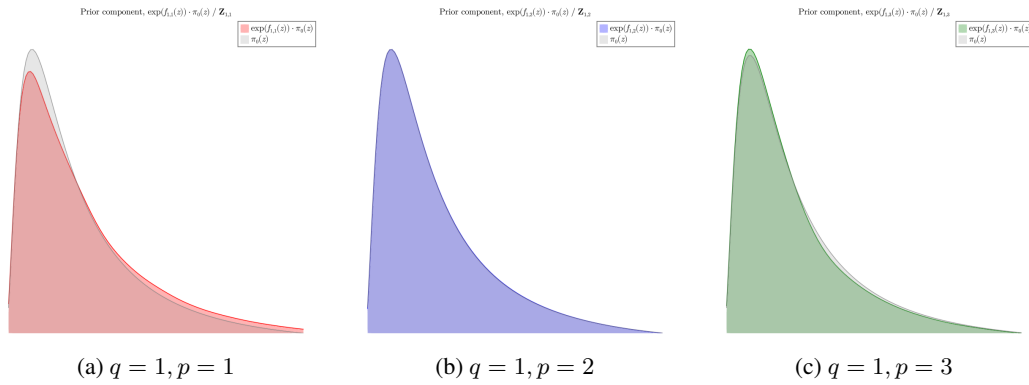


Figure 24: Three components from T-KAM's prior after training on FMNIST for 5,000 parameter updates with RBF bases and lognormal constrained priors.

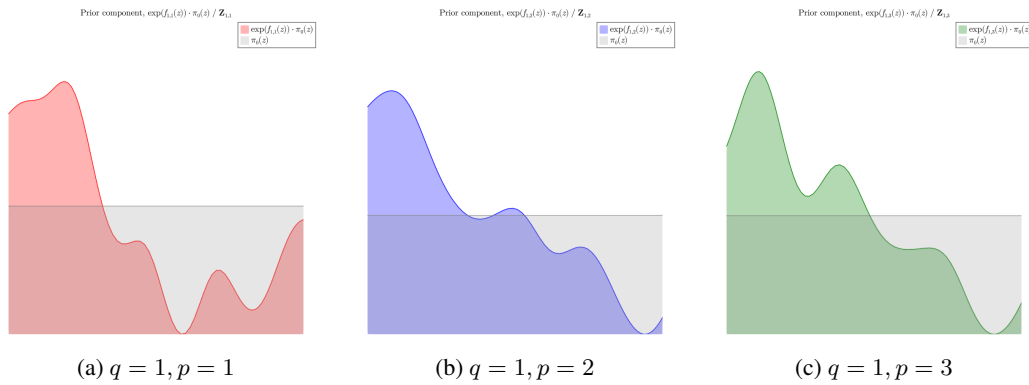


Figure 25: Three components from T-KAM's prior after training on FMNIST for 5,000 parameter updates with RBF bases and uniform constrained priors.

A.8.4 FMNIST FFT

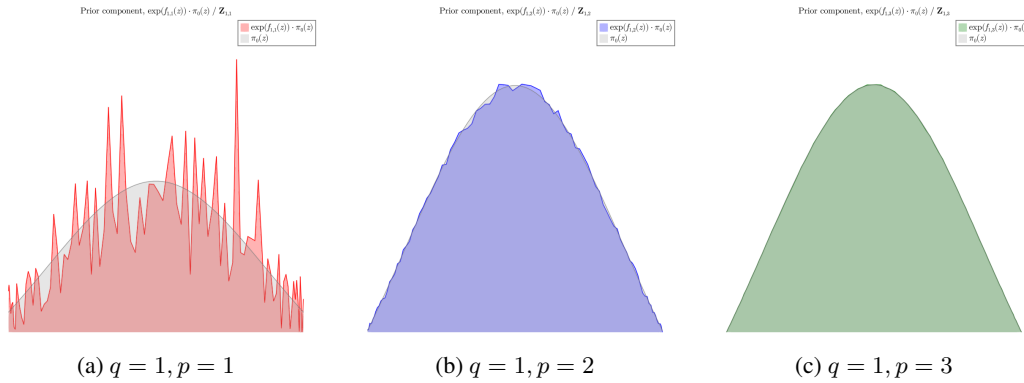


Figure 26: Three components from T-KAM's prior after training on FMNIST for 5,000 parameter updates with FFT bases and Gaussian constrained priors.

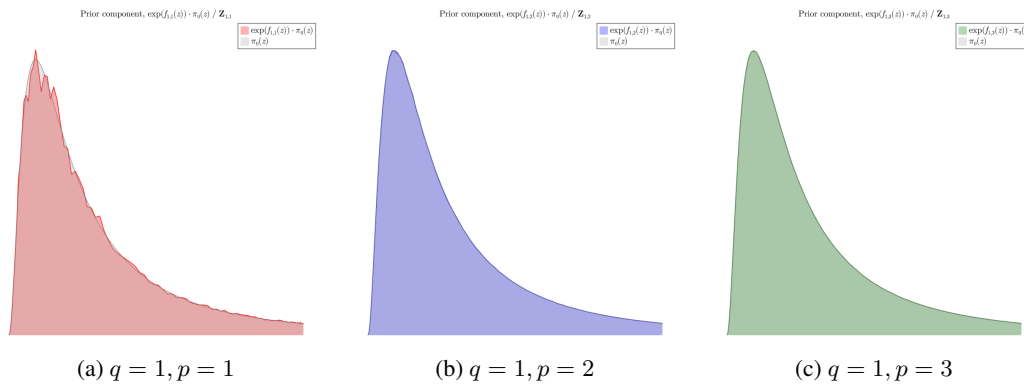


Figure 27: Three components from T-KAM's prior after training on FMNIST for 5,000 parameter updates with FFT bases and lognormal constrained priors.

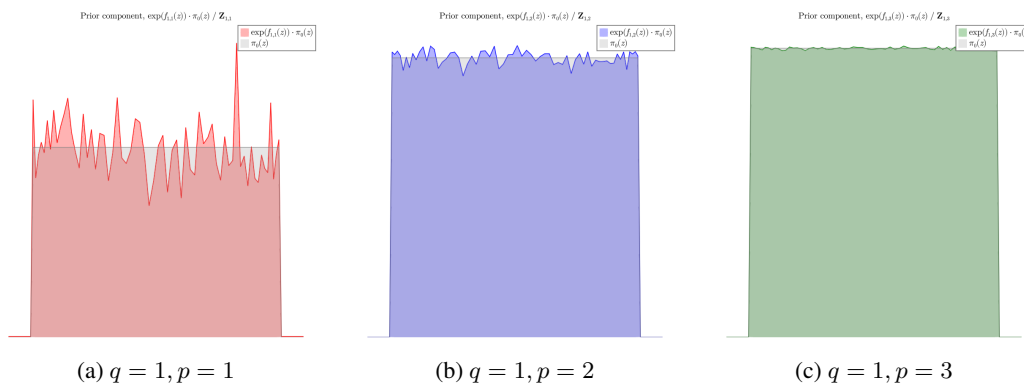


Figure 28: Three components from T-KAM's prior after training on FMNIST for 5,000 parameter updates with FFT bases and uniform constrained priors.

A.8.5 DARCY RBF

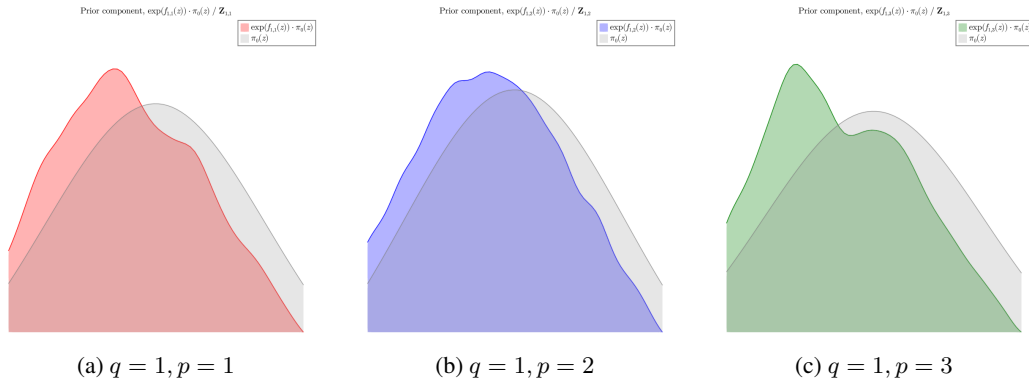


Figure 29: Three components from T-KAM's prior after training on Darcy flow pressures for 10,000 parameter updates with RBF bases and Gaussian constrained priors.

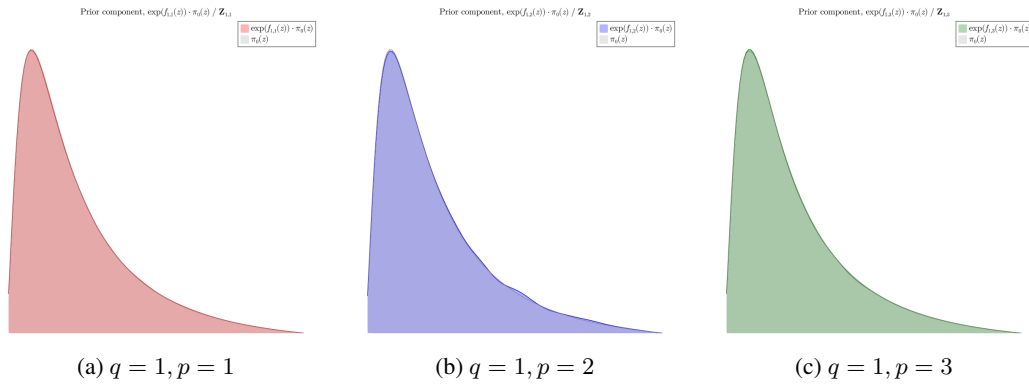


Figure 30: Three components from T-KAM's prior after training on Darcy flow pressures for 10,000 parameter updates with RBF bases and lognormal constrained priors.

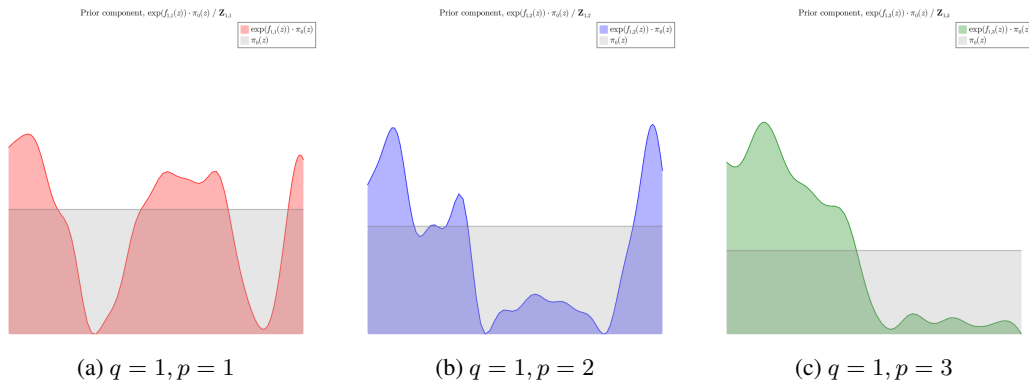


Figure 31: Three components from T-KAM's prior after training on Darcy flow pressures for 10,000 parameter updates with RBF bases and uniform constrained priors.

A.8.6 DARCY FFT

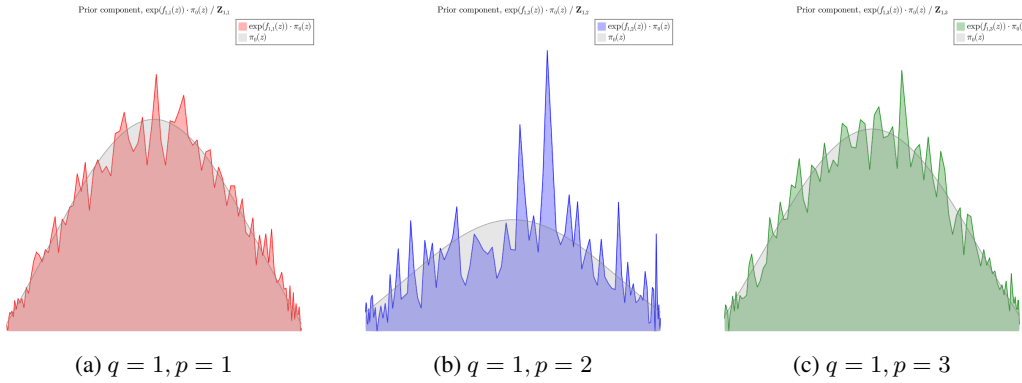


Figure 32: Three components from T-KAM's prior after training on Darcy flow pressures for 10,000 parameter updates with FFT bases and Gaussian constrained priors.

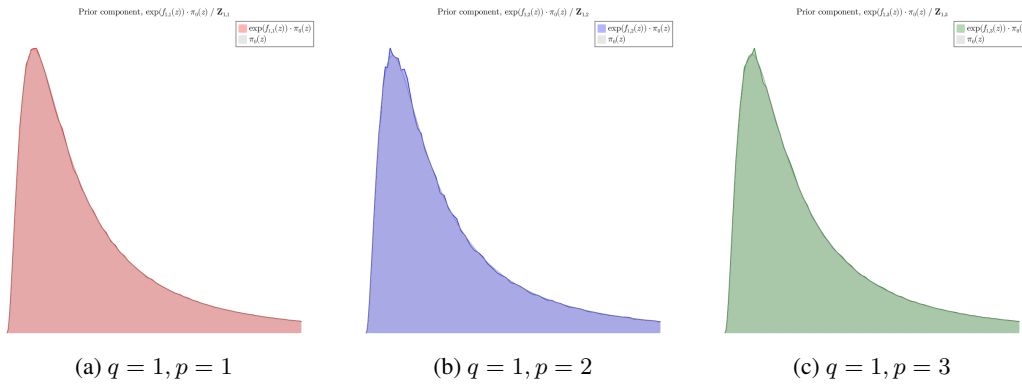


Figure 33: Three components from T-KAM's prior after training on Darcy flow pressures for 10,000 parameter updates with FFT bases and lognormal constrained priors.

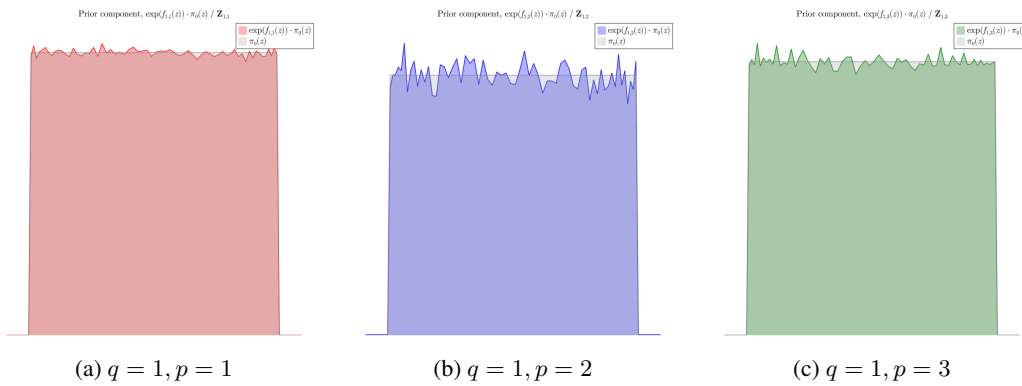


Figure 34: Three components from T-KAM's prior after training on Darcy flow pressures for 10,000 parameter updates with FFT bases and uniform constrained priors.